Chapter 5

ELECTROCHEMICAL CORROSION AND WEAR BEHAVIOUR

This chapter presents the results obtained from electrochemical corrosion testing, including open circuit potential (OCP), electrochemical impedance spectroscopy (EIS), and potentiodynamic polarization (PDP), as well as tribological studies focusing on friction, wear, and wear mechanisms. It provides a comparative analysis of the corrosion and wear behavior among different sets of alloys.

5.1 Electrochemical corrosion behaviour

5.1.1 Corrosion behaviour of cpTi and Ti-6Al-4V

The electrochemical impedance spectroscopy (EIS) study was carried at OCP, which provides insights into the corrosion resistance and surface behavior of the cpTi and Ti-6Al-4V alloys in SBF environments. The Nyquist plots from the EIS analysis shown in Fig. 5.1(a) revealed that the cpTi has a single capacitive semicircle, indicating the formation of a stable and uniform passive oxide layer on the surface. The larger diameter of the semicircle suggests higher charge transfer resistance (R_{ct}), indicative of excellent corrosion resistance.

The Ti-6Al-4V alloy also exhibited a similar capacitive loop but with a smaller semicircle diameter compared to cpTi. This difference points to a lower R_{ct}, suggesting slightly reduced corrosion resistance as given in Table 5.1, due to potential microstructural inhomogeneities or alloying effects. Both cpTi and Ti-6Al-4V displayed a single capacitive semicircle, indicating the formation of a stable and uniform passive oxide layer on the surface. The larger diameter of the semicircle suggests higher charge transfer resistance (R_{ct}), indicative of excellent corrosion resistance.

The Bode plots shown in Fig. 5.1(b) shows higher impedance values for cpTi across a wide frequency range, while the phase angle plots exhibited a broad peak near -80° in the intermediate frequency region, indicating robust capacitive behavior and superior passive film stability compared to the narrower phase peak of Ti-6Al-4V. The impedance data, modeled using an equivalent circuit shown in Fig. 5.1(d) comprising solution resistance (R_s), a constant phase element (*CPE*), and charge transfer resistance (R_{ct}), revealed that cpTi exhibited higher R_{ct} and lower *CPE* values indicative of a thick and well-formed passive oxide layer, whereas Ti-6Al-4V showed reduced R_{ct} and higher *CPE* values, reflecting a thinner and less protective passive layer.

The Tafel plots for cpTi and Ti-6Al-4V are shown in Fig. 5.1(c) and the corresponding corrosion parameters including corrosion potential (E_{corr}), corrosion current density (I_{corr}), and corrosion rate are given in Table 5.2. The corrosion potential (E_{corr}) for cpTi is –0.1301 V, which is more noble compared to Ti-6Al-4V (-0.3135 V). This indicates that cpTi exhibits a higher resistance to corrosion initiation under the test conditions. The corrosion current density (I_{corr}) for cpTi is 0.7262 μA/cm^2, which is significantly lower than the Ti-6Al-4V (1.4382μA/cm^2), reflecting a reduced rate of electrochemical reaction for cpTi. Correspondingly, the corrosion rate for cpTi (0.0063 mm/year) is lower than Ti-6Al-4V (0.0126 mm/year), demonstrating that cpTi exhibits superior corrosion resistance compared to the Ti-6Al-4V alloy.

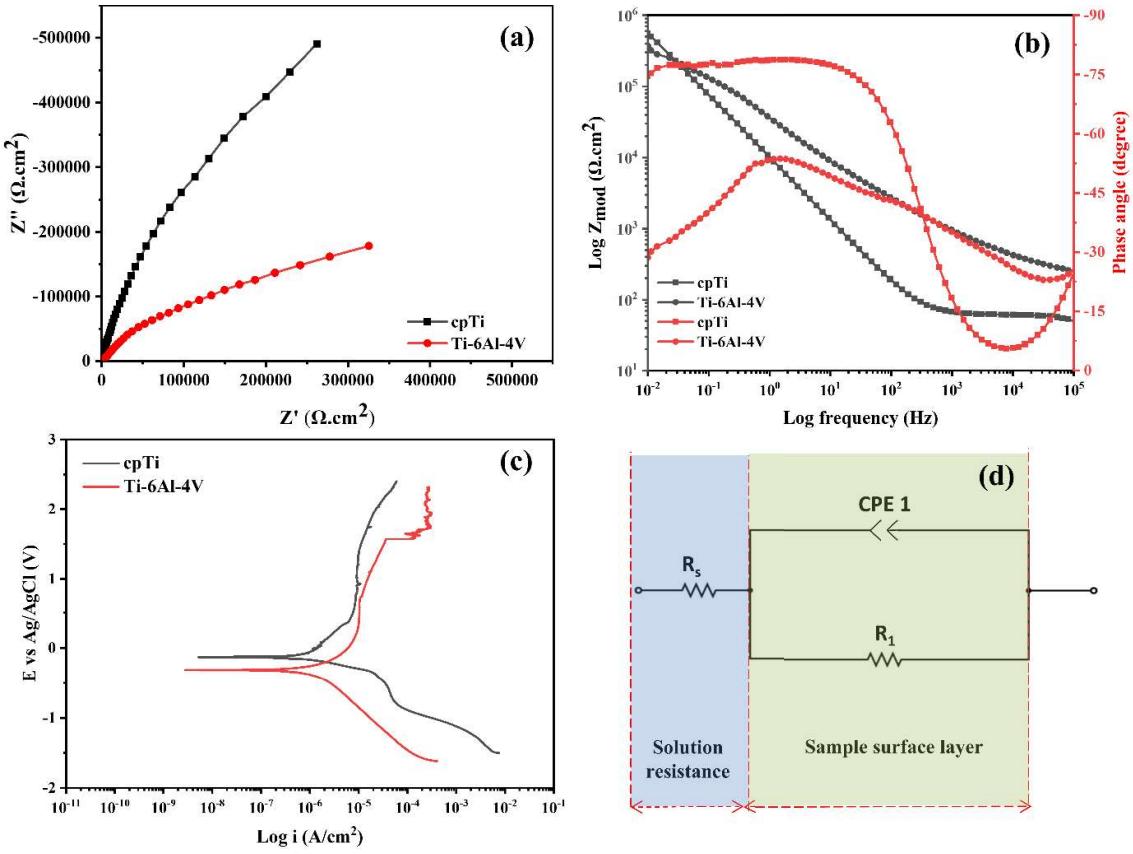

Fig. 5.1: Corrosion response of cpTi and Ti-6Al-4V (a) Nyquist plot, (b) Bode plot, (c) Tafel plot, and (d) Equivalent circuit diagram

Table 5.1: Impedance parameters derived from EIS fitting for cpTi and Ti-6Al-4V alloys

Sample	Rs (Ω.cm^2)	CPE$_1$ ($10^{-6}\Omega^{-1}$.cm^{-2}.s^n)	R$_1$ (Ω.cm^2) ×10^6	n$_1$	χ^2 (10^{-3})
cpTi	59.11 ± 3.18	19.55 ± 1.01	(1.63 ± 0.07)	0.89	2.0
Ti-6Al-4V	61.21 ± 5.18	10.07 ± 0.89	(0.83± 0.05)	0.57	4.4

Table 5.2: Corrosion parameters obtained from Tafel extrapolation for cpTi and Ti-6Al-4V alloys

Sample	E_{corr} (V)	I_{corr} (µA/cm^2)	Corrosion rate (mm/year)
cpTi	-0.1301 ± 0.007	0.7262 ± 0.006	0.0063
Ti-6Al-4V	-0.3135 ± 0.015	1.4382 ± 0.013	0.0126

5.1.2 Corrosion behaviour of sintered binary alloys

The results obtained from the EIS are displayed in Figs. 5.2(a) and 5.2(b) as a Nyquist and Bode plot. The qualitative and general perspective for comparing Nyquist plots of different samples involves evaluating the diameter of the semicircular arc plotted between the imaginary and real components of impedance. Greater arc diameter indicates higher corrosion resistance, while smaller arc diameter suggests lower corrosion resistance [212,213]. In Fig. 5.2(a), the arc diameter of cpTi is largest among all samples. While, all Ti-Nb alloys shows less arc diameter than cpTi, which represent a lower corrosion resistance. Among developed samples, Ti-5Nb and Ti-10Nb shows largest arc diameter, indicating the highest corrosion resistance among Ti-Nb alloys. Additionally, it is noted that increase in Nb content reduces the arc diameter as well as resistance against corrosion of the alloy, which is evident in Nyquist plot shown in Fig. 5.2(a). In addition, the Bode plot shown on double Y-axis represents the impedance modulus against the frequency on the logarithmic scale and phase angle against the logarithmic frequency. In this Bode impedance plot, the impedance modulus of Ti-Nb alloys reaches up to 10^5, which is significantly lower than cpTi, having impedance modulus reaches up to 10^6. The Ti-Nb alloys shows lower impedance modulus than cpTi, which represents a lower corrosion resistance than cpTi. The phase angle of cpTi also reaches 79° in the lower and medium frequency range, which supports the results

of Nyquist and Bode impedance plot. As the angle increases in the lower and medium frequency range, the corrosion resistance also increases, and vice versa. Other alloys in the present study have lower phase angle than cpTi, which denotes their lower corrosion resistance.

To further quantify the impedance parameter, the results of EIS have been examined by fitting them to the analogous circuit design shown in Fig. 5.2(d). Here, Fig. 5.2(d) represent the equivalent circuit for represents for all Ti-Nb alloys. The impedance parameter obtained from the curve fitting with the help of Zstudio are shown in Table 5.3. In this table, "R_s" denotes the solution resistance, "R_1" signifies the resistance of the outer porous layer, "R_2" indicates the resistance of the inner barrier layer, while "CPE_1" and "CPE_2" represent the capacitance of the outer and inner layers respectively. In Ti-Nb alloys, R_1 is also highest for cpTi. While, all Ti-Nb alloys having lower R_1 value than cpTi, which validates the qualitative results described through Nyquist and Bode plot.

Furthermore, the corrosion behavior of Ti-Nb alloys is quantitatively analyzed through the PDP test, and findings are depicted through Tafel plots shown in Fig. 5.2(c). It's noted that the corrosion potential of cpTi is higher contrastingly with the Ti-Nb alloys. Although Ti-5Nb alloy exhibits highest corrosion potential among developed alloys, while Ti-25Nb shows the lowest among all. In all sample passivation and re-passivation zone obtained in the anodic region which indicate the development of corrosion resistant passivation layer [214]. Furthermore, for more effective comparison of corrosion potential and corrosion rate, PDP parameters were determined using the Tafel extrapolation technique and values are provided in Table 5.4. The corrosion current density (I_{corr}) is seen to be minimal for cpTi. Consequently, the corrosion rate for cpTi is the lowest, while the corrosion rate increases with higher Nb concentration in Ti-Nb

alloys.

In this present study, EIS analysis of Ti-xZr alloys has been done to delve deeper into their corrosion behavior. The results of the EIS test are illustrated using the Nyquist and Bode plot, which is presented in Figs. 5.3(a) and 5.3(b). In the context of Nyquist plots, a pivotal parameter for evaluating corrosion resistance is the diameter of this semicircular arc, which directly correlates with corrosion behavior [215]. Notably, as evident in Fig. 5.3(a), the semicircle diameters observed in the Ti-20Zr alloy are substantially larger than the remaining three samples, indicating the highest impedance. On the contrary, the arc diameter in Ti-5Zr is notably reduced in comparison to the other specimens. The Bode plot depicted in Fig. 5.3(b) demonstrates that, at lower to moderate frequency, three titanium-zirconium alloys exhibit a phase angle in the range of 57° to 72°, with the exception of Ti-5Zr. This finding suggests that when these alloys are submerged in the solution, they display capacitive activity and establishment of a very stable oxide layer on their surface. As the frequency rises to 10^3-10^5 Hz, the impedance modulus of all alloys remains constant, accompanied with a decrease in the phase angle on the Bode plot, suggesting a reaction attributed to solution resistance. Furthermore, the slope of the impedance modulus approaches -1 in the middle and lower frequency ranges, indicating the alloy's impedance's supremacy over the solution's resistance. As Fig. 5.3(b) illustrates, the profiles of Ti-15Zr and Ti-20Zr are somewhat comparable, indicating that the corrosion behavior of these two alloys is consistent even in solutions with lower pH values. Furthermore, there is a little phase angle resemblance between the profiles of Ti-10Zr and Ti-15Zr and Ti-20Zr. However, the spectral profile of Ti-5Zr exhibits notable changes towards a reduced phase angle, indicating a potentially reduced protective passive film on the surface of Ti-5Zr. It is important to note that any inferences made from the EIS graphs should be considered

speculative, as these Bode-phase graphs do not offer precise insights into the electrochemical performance of Ti-Zr. Based on qualitative observations from the experiment, it can be inferred that every Ti-Zr sample studied exhibit at least two-time constants and the similar double-layer deposition. This demonstrates the similarity in the production of a titanium oxide layer and the corrosion dynamics of all the Ti-Zr alloys under study. Two layers of protection are usually present in titanium alloys: an exterior porous layer and an interior barrier layer [216,217]. Furthermore, ZView® software was employed to evaluate the impedance characteristics, utilizing the "equivalent circuit" illustrated in Fig. 5.3 (d). The results obtained from EIS were quantitatively validated through this approach. Conforming to this model, an oxide layer on Ti-Zr alloys is hypothesized to consist of an outer porous layer and an inner barrier-like layer. The resistances associated with the SBF, outer porous layer (R_1), and inner barrier-like layer (R_2) are indicated in this representation by R_S, R_1, and R_2, respectively. Additionally, CPE_1 represents the capacitance of the outer porous layer, and CPE_2 represents the capacitance of the inner barrier layer. To simplify the representation and account for deviations from ideal capacitor behavior, a constant-phase element (*CPE*) was used instead of actual capacitance [218]. The impedance of the phase element (Z_{CPE}) is expressed as $[C(I\omega)^n]^{-1}$, where C, I, and ω stand for capacitance, current, and frequency, respectively, and n is a value ranging from -1 to 1. The value of n is linked to variations in current distribution caused by surface imperfections and roughness [219,220]. Table 5.5 presents the derived values for capacitance, resistance, and the parameter 'n' obtained by fitting the experimental data to the "equivalent circuit" for both the inner and outer layers. When n approaches a value of one, it signifies that the characteristics of such a layer closely resemble those of an ideal capacitor [221]. To evaluate the goodness of fit, chi-square (χ^2) values,

which consistently fell within the range of 10^{-3}, were utilized, indicating a strong conformity of the data to the suggested predictive circuit.

The external porous layer resistance in Ti-5Zr measures 1.08×10^5 Ω cm^2, representing the lowest value when compared to the other three alloys. This implies that the Ti-5Zr alloy demonstrates reduced stability in a corrosive environment. On the other hand, Ti-20Zr has the highest resistance of its outer porous layer (R_1), indicating that this layer exhibits greater resistant to the SBF compared to the other alloys. The resistance provided by the inner barrier layer (R_2) is somewhat greater than the R_1, suggesting that the inner barrier layer is more corrosion-resistant. In context of Zr addition, Ti-5Zr shows the lowest while Ti-20Zr shows the highest resistance value of R_2. Moreover, it is reported that corrosion protection is attributed to both protective layers [222]. A comparison between the capacitances CPE_1 (related with the outer porous layer) and CPE_2 (associated with the inner barrier layer) for the various Ti-Zr alloys was done within the framework of the suggested equivalent circuit. Remarkably, the observed values of capacitance CPE_2, which is associated with the inner barrier layer in all Ti-Zr alloys, were lower than those of CPE_1. The literature has previously indicated that a thicker barrier of protection is linked to the observed lower capacitances [223–225].

The potentiodynamic polarization curves for the produced Ti-Zr alloys are displayed in Fig. 5.3(c), and Table 5.6 lists the values derived from the Tafel experiments. The findings show that Ti-5Zr alloy has the greatest value of corrosion current density (I_{corr}). Consequently it will offer lowest resistance to corrosion among the developed alloys as corrosion rate is directly proportional to I_{corr} [226]. Moreover, the Zr addition greater than 5 wt.% reduces the I_{corr} from 0.53103 μA/cm^2 (Ti-5Zr) to 0.36921 μA/cm^2 (Ti-10Zr), 0.15458 μA/cm^2 (Ti-15Zr), and 0.13388 μA/cm^2 (Ti-20Zr), respectively. Subsequently, the corrosion rate, which is directly proportional to I_{corr}, is decreasing in

the similar manner to I_{corr}. The highest corrosion rate of 0.00496 mm/year have been observed for 5% Zr contained sample. While it is observed to have a reduction in corrosion rate for Ti-10Zr to Ti-20Zr alloys. The lowest corrosion rate of 0.00129 mm/year have obtained for Ti-20Zr alloy. Although, the Ti-15Zr alloys also showed somewhat similar corrosion rate of 0.00146 mm/year.

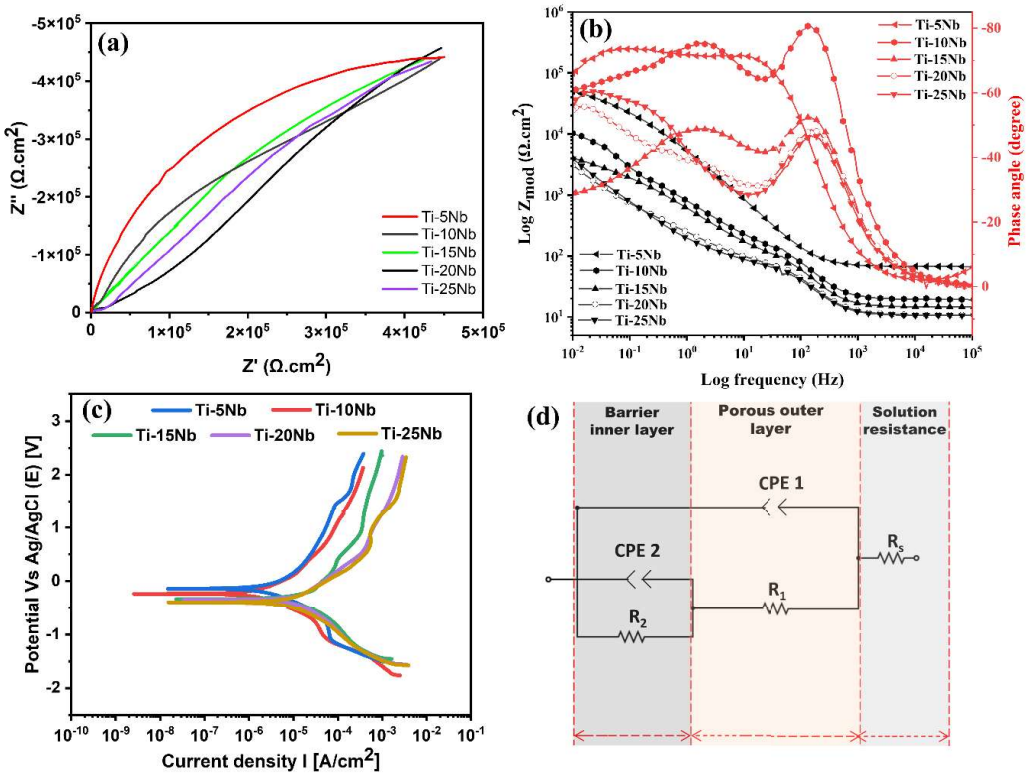

Fig. 5.2: Corrosion response of Ti-xNb alloys (a) Nyquist plot, (b) Bode plot, (c) Tafel plot, and (d) Equivalent circuit diagram

Table 5.3: Impedance parameters derived from EIS fitting for Ti-xNb alloys

Sample	R_S ($\Omega.cm^2$)	CPE_1 ($10^{-6}\Omega^{-1}.cm^{-2}.s^n$)	R_1 ($\Omega.cm^2$)	n_1	CPE_2 ($10^{-6}\Omega^{-1}.cm^{-2}.s^n$)	R_2 ($\Omega.cm^2$)	n_2	$\chi^2 \times 10^{-3}$
Ti-5Nb	59.44 ± 3.23	26.98 ± 1.16	4121 ± 118	0.92	33.36 ± 0.78	139058 ± 131	0.91	1.1
Ti-10Nb	66.71 ± 4.11	30.41 ± 1.67	2008 ± 82	0.90	65.876 ± 2.13	123990 ± 112	0.89	2.0
Ti-15Nb	14.65 ± 1.18	50.42 ± 2.18	113.8 ± 6.05	0.97	277.76 ± 8.11	26996 ± 418	0.94	0.6
Ti-20Nb	10.64 ± 0.39	54.77 ± 2.47	66.42 ± 3.21	0.95	1775.4 ± 21.18	18432 ± 327	0.93	6.3
Ti-25Nb	10.50 ± 0.21	62.05 ± 3.11	68.77 ± 5.14	0.93	1772.2 ± 23.18	21345 ± 234	0.91	1.3

Table 5.4: Corrosion parameters obtained from Tafel extrapolation for Ti-xNb alloys

Sample	E_{corr} (V)	I_{corr} ($\mu A/cm^2$)	Corrosion rate (mm/year)
Ti-5Nb	-0.2349 ± 0.019	0.7715 ± 0.009	0.0075
Ti-10Nb	-0.2385 ± 0.011	0.8410 ± 0.008	0.0082
Ti-15Nb	-0.3347 ± 0.018	5.4328 ± 0.008	0.0534
Ti-20Nb	-0.3481 ± 0.018	8.3373 ± 0.008	0.0829
Ti-25Nb	-0.3932 ± 0.018	6.4017 ± 0.008	0.0633

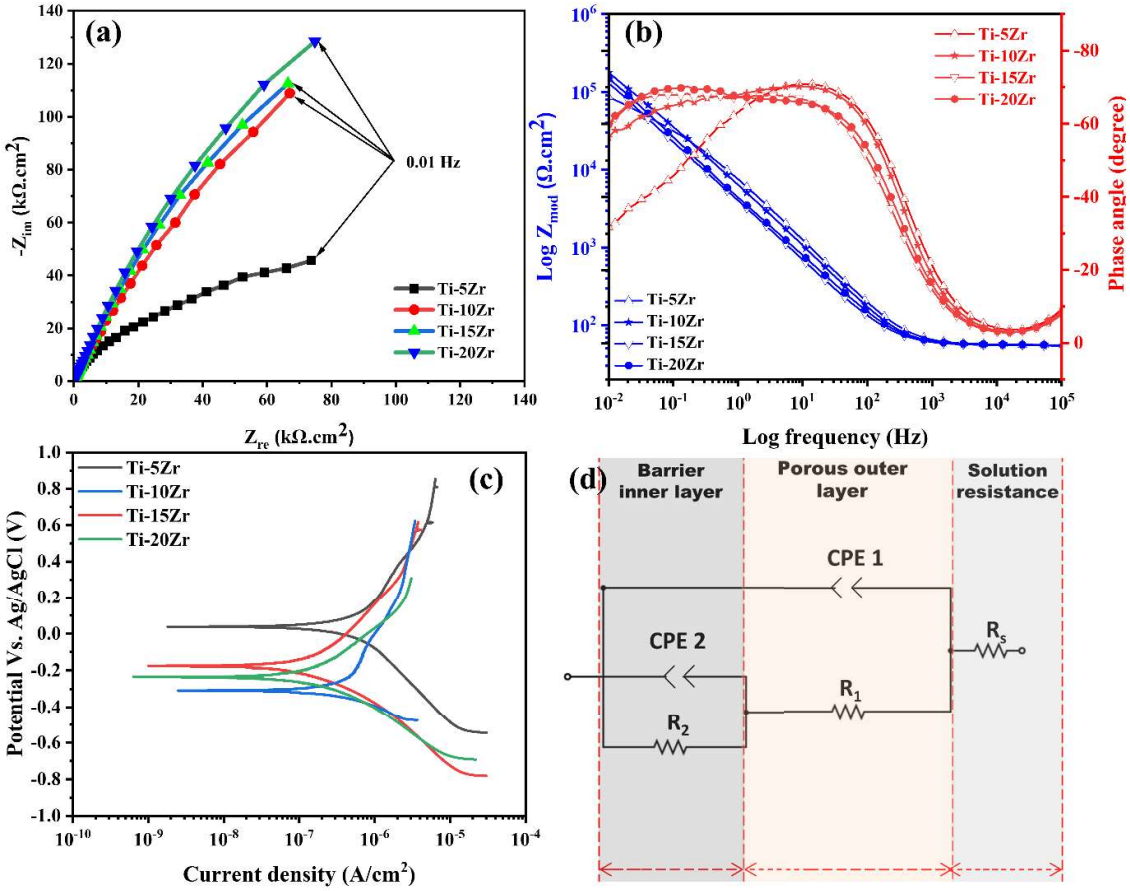

Fig. 5.3: Corrosion response of Ti-xZr alloys (a) Nyquist plot, (b) Bode plot, (c) Tafel plot, and (d) Equivalent circuit diagram

Table 5.5: Impedance parameters derived from EIS fitting for Ti-xZr alloys

Sample	R_S (Ω.cm^2)	CPE_1 (10^{-6}Ω^{-1}.cm^{-2}.s^n)	R_1 (Ω.cm^2)	n_1	CPE_2 (10^{-6}Ω^{-1}.cm^{-2}.s^n)	R_2 (Ω.cm^2)	n_2	$\chi^2 \times 10^{-3}$
Ti-5Zr	55.37	49.88	1.08×10^4	0.86	27.22	3.66×10^5	0.79	2.4
Ti-10Zr	54.14	36.85	1.70×10^4	0.81	19.01	6.29×10^5	0.75	2.3
Ti-15Zr	54.96	23.42	0.49×10^5	0.87	18.04	7.67×10^5	0.71	1.9
Ti-20Zr	55.37	22.35	0.56×10^5	0.84	15.21	1.35×10^6	0.73	2.5

Table 5.6: Corrosion parameters obtained from Tafel extrapolation for Ti-xZr alloys

Sample	E_{corr} (v)	I_{corr} (μA/cm^2)	Corrosion rate (mm/year)
Ti-5Zr	0.034	0.531	0.00496
Ti-10Zr	-0.305	0.369	0.00352
Ti-15Zr	-0.171	0.155	0.00146
Ti-20Zr	-0.233	0.134	0.00129

5.1.3 Corrosion behaviour of sintered ternary alloys

The corrosion behaviour of ternary Ti-10Zr-xNb alloys were analyzed through EIS and PDP tests and the obtained results are presented in the form of Nyquist plots in Fig. 5.4(a), Bode plots in Fig. 5.4(b), Tafel plots in Fig. 5.4(c), and the equivalent circuit diagram for EIS fitting in Fig. 5.4(d). The corresponding quantitative values of impedance and corrosion parameters are presented in Table 5.7 and Table 5.8. The Nyquist plot shows semicircles corresponding to the impedance of the alloys. Ti-10Zr-5Nb exhibits the largest semicircle diameter, indicating the highest charge transfer resistance (R_2) and superior corrosion resistance due to the formation of a dense and protective oxide layer. As the Nb content increases (Ti-10Zr-15Nb and Ti-10Zr-20Nb), the semicircles shrink, suggesting a reduction in the protective barrier's effectiveness.

The Bode plot shows that the impedance modulus $|Z|$ values are higher for Ti-10Zr-5Nb across the frequency range, confirming its superior corrosion resistance. The phase angle for Ti-10Zr-5Nb is also higher than the other alloys at intermediate frequencies, signifying more capacitive behavior and a stable passive film. Alloys with higher Nb content (15Nb and 20Nb) show lower $|Z|$ and less pronounced phase angles, indicating compromised corrosion protection. Table 5.7 presents the impedance parameters derived from EIS fitting for Ti-10Zr-xNb alloys, highlighting the electrochemical behavior and surface properties of the alloys. The solution resistance (R_s) remains

relatively consistent across all compositions, indicating similar electrolyte properties. However, significant variations in charge transfer resistance (R_1, R_2) and constant phase elements (CPE_1, CPE_2) values are observed. Ti-10Zr-5Nb exhibits the highest R_2 (2.35 × 10^3 Ω.cm²), indicative of superior corrosion resistance compared to other compositions, likely due to the formation of a stable passive film. The decrease in R_1 and R_2 values for higher Nb content (15Nb and 20Nb) suggests diminished protective oxide layer integrity.

Furthermore, the polarization curves in Fig. 5.4(c) highlight that Ti-10Zr-5Nb has the lowest corrosion current density (I_{corr}) and the highest corrosion potential (E_{corr}), signifying better corrosion resistance compared to the other compositions. Increasing Nb content shifts the curves toward higher I_{corr} and lower E_{corr} values, reflecting reduced resistance to corrosion. The corresponding values of E_{corr} and I_{corr} is given in Table 5.8. The Ti-10Zr-5Nb has the highest E_{corr} value (-0.0361 V), indicating the most noble behavior and suggesting a greater resistance to corrosion initiation. As the Nb content increases, the E_{corr} values become more negative (e.g., -0.2035 V for Ti-10Zr-20Nb), reflecting increased susceptibility to corrosion. The corrosion rate follows a similar trend, with Ti-10Zr-5Nb showing the lowest rate (0.207 mm/year), confirming its superior corrosion resistance. Ti-10Zr-20Nb has the highest corrosion rate (1.093 mm/year), which aligns with its higher I_{corr} and more negative E_{corr} values, highlighting its poorer corrosion resistance.

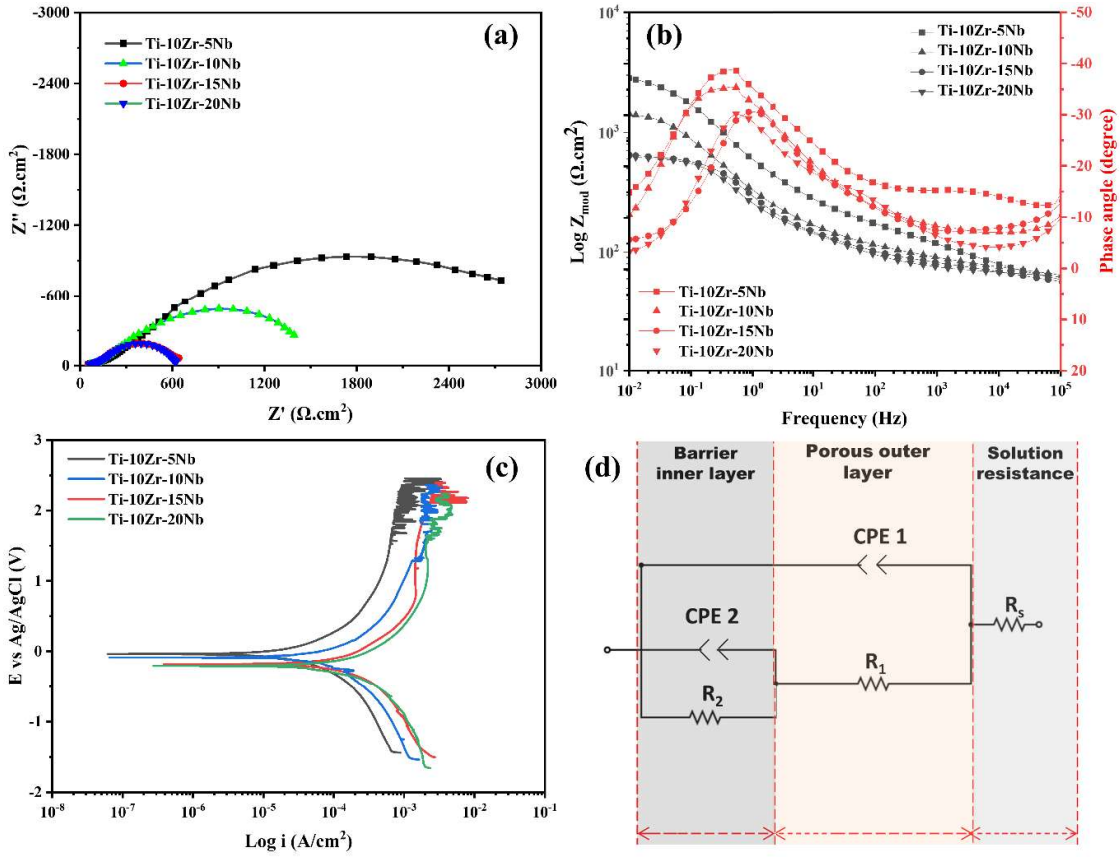

Fig. 5.4: Corrosion response of Ti-10Zr-xNb alloys (a) Nyquist plot, (b) Bode plot, (c) Tafel plot, and (d) Equivalent circuit diagram

Table 5.7: Impedance parameters derived from EIS fitting for Ti-10Zr-xNb alloys

Sample	R_S ($\Omega.cm^2$)	CPE_1 ($10^{-3}\Omega^{-1}.cm^{-2}.s^n$)	R_1 ($\Omega.cm^2$) $\times 10^3$	n_1	CPE_2 ($10^{-3}\Omega^{-1}.cm^{-2}.s^n$)	R_2 ($\Omega.cm^2$) $\times 10^3$	n_2	χ^2 $\times 10^{-3}$
Ti-10Zr-5Nb	35.41	21.2	0.98	0.18	8.19	2.35	0.75	0.4
Ti-10Zr-10Nb	34.27	7.55	0.70	0.11	11.18	0.44	0.78	0.3
Ti-10Zr-15Nb	34.34	5.27	0.49	0.14	1.43	1.32	0.71	0.8
Ti-10Zr-20Nb	35.65	7.55	0.56	0.14	1.46	0.44	0.73	7.2

Table 5.8: Corrosion parameters obtained from Tafel extrapolation for Ti-10Zr-xNb alloys

Sample	E_{corr} (V)	I_{corr} (μA/cm^2)	Corrosion rate (mm/year)
Ti-10Zr-5Nb	-0.0361	17.24	0.207
Ti-10Zr-10Nb	-0.0971	48.92	0.584
Ti-10Zr-15Nb	-0.1748	84.51	0.998
Ti-10Zr-20Nb	-0.2035	95.22	1.093

5.1.4 Corrosion behaviour of sintered high entropy alloys

The corrosion behavior of high-entropy alloys (HEA Sn and HEA Cu) is illustrated in the Fig. 5.5. Figure 5.5(a) shows the Nyquist plot, which shows a larger semicircle for HEA Sn than HEA Cu, suggesting that HEA Sn has higher charge transfer resistance (R_2). This indicates better corrosion resistance and a more stable passive layer compared to HEA Cu. In the Bode plot shown in Fig. 5.5(b), HEA Sn exhibits a higher impedance modulus $|Z|$ across the frequency spectrum, indicating superior corrosion protection. The phase angle for HEA Sn is also higher than the HEA Cu in the mid-frequency range, reflecting capacitive behavior and a well-formed passive oxide film. HEA Cu shows lower $|Z|$ and less pronounced phase angles, suggesting less effective corrosion resistance than HEA Cu. The impedance parameter obtained from the fitting are given in Table 5.9. The circuit diagram for porous high entropy alloys also illustrates the electrochemical response with two constant phase elements (CPE_1 and CPE_2) representing the porous outer and dense barrier inner layers, respectively. The larger R_2 for HEA Sn implies a more effective barrier layer that enhances its corrosion resistance compared to HEA Cu.

Furthermore, the polarization curves shown in Fig. 5.5(c) and corresponding values in Table 5.10 indicate that HEA Sn has more positive corrosion potential (E_{corr}) and a lower corrosion current density (I_{corr}) compared to HEA Cu. This signifies that HEA Sn is less susceptible to corrosion. HEA Cu, with higher I_{corr} and more negative E_{corr}, exhibits poorer corrosion than HEA Cu.

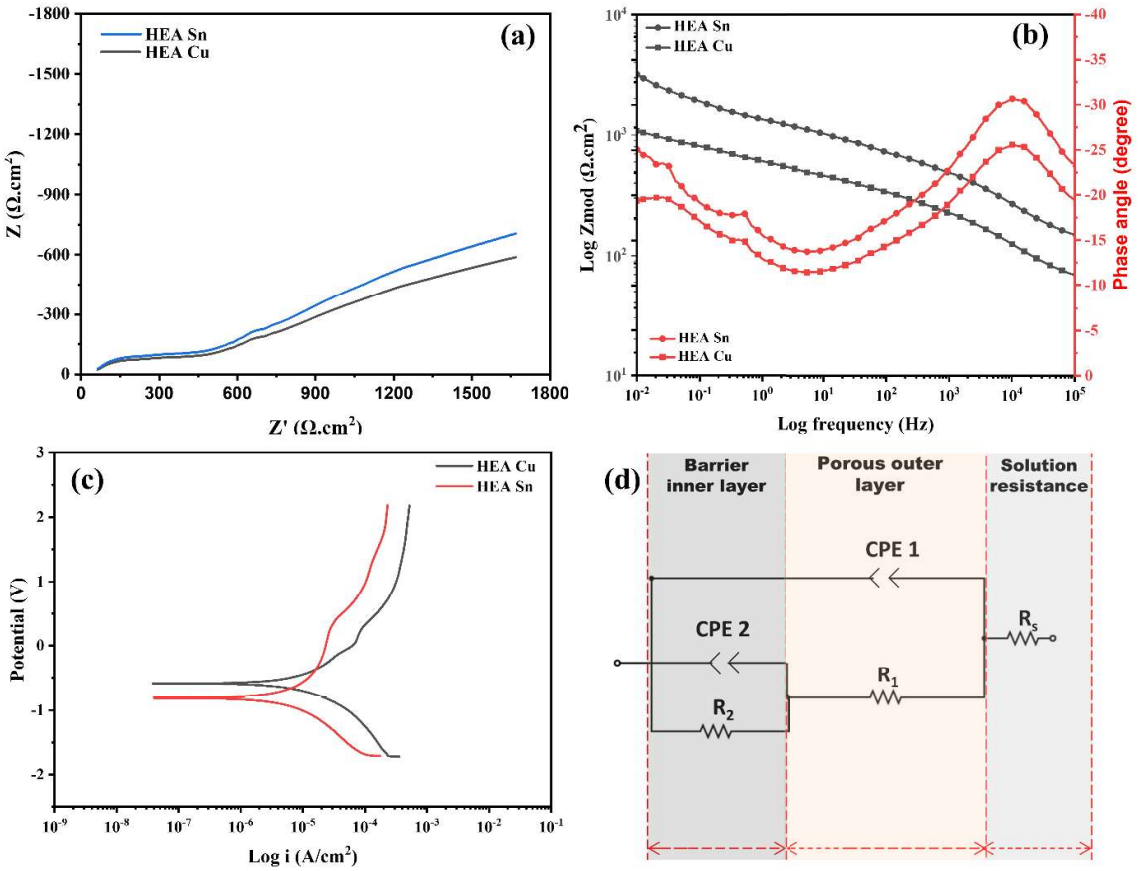

Fig. 5.5: Corrosion response of high entropy alloys (a) Nyquist plot, (b) Bode plot, (c) Tafel plot, and (d) Equivalent circuit diagram

Table 5.9: Impedance parameters derived from EIS fitting for high entropy alloys

Sample	R_S ($\Omega.cm^2$)	CPE_1 ($10^{-6}\Omega^{-1}.cm^{-2}.s^n$)	R_1 ($\Omega.cm^2$) $\times 10^3$	n_1	CPE_2 ($10^{-6}\Omega^{-1}.cm^{-2}.s^n$)	R_2 ($\Omega.cm^2$) $\times 10^3$	n_2	χ^2 $\times 10^{-3}$
HEA Cu	24.32	1.236	0.51	0.46	27.22	3.66	0.59	2.4
HEA Sn	26.16	0.815	0.56	0.42	19.71	3.99	0.43	1.6

Table 5.10: Corrosion parameters obtained from Tafel extrapolation for high entropy alloys

Sample	E_{corr} (V)	I_{corr} ($\mu A/cm^2$)
$TiNb_{1.5}Mo_{1.1}Zr_{1.15}Cu_{0.25}$	-0.3787	5.281
$TiNbZr_{0.8}Mo_{0.92}Sn_{0.28}$	-0.8145	2.708

5.1.5 Corroded surface study

The SEM images of corroded surface of cpTi and Ti-6Al-4V are shown in Fig. 5.6. It is observed that cpTi has uniform corrosion and no such large pits were observed in Fig. 5.6(a). This indicates the minimal corrosion activity and reflects the natural ability of cpTi to form a protective passive oxide layer (TiO_2) that resists corrosion. On the other hand, the SEM image of corroded surface of Ti-6Al-4V shows minor pits of white colour which is the oxides of Al and V. The presence of aluminium (Al) and vanadium (V) in Ti-6Al-4V can influence the stability of the passive oxide layer. Under aggressive environments, these alloying elements might contribute to localized corrosion, such as pitting or crevice corrosion, especially at defects or scratches.

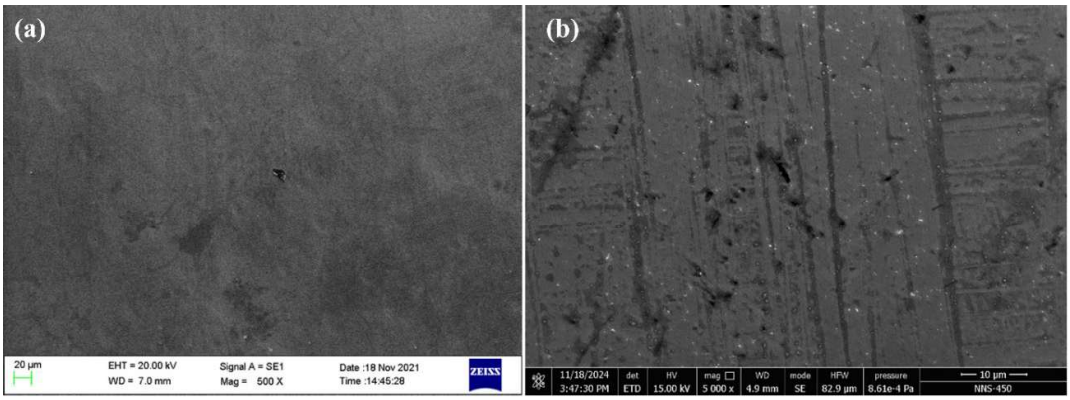

Fig. 5.6: SEM images of corroded surface of (a) cpTi and (b) Ti-6Al-4V

The SEM images of the corroded surfaces of Ti-xNb alloys, presented in Fig. 5.7, provide a detailed understanding of the corrosion mechanisms and surface characteristics of these alloys. The images reveal the formation of corrosion-induced oxides, which appear prominently in white, indicating their distribution across the surface. These oxides predominantly consist of titanium dioxide (TiO_2) and niobium pentoxide (Nb_2O_5), both of which are known for their high stability and protective nature. The formation of these oxides plays a crucial role in enhancing the corrosion resistance of the alloy by forming a passive layer that limits further interaction with the corrosive environment. A notable observation from the SEM micrographs is that the corrosion tends to be more progressive near the porous regions of the material. This can be attributed to the higher surface area and increased exposure of these areas to the corrosive medium, which accelerates localized electrochemical reactions. In contrast, the regions away from the pores remain largely unaffected and exhibit no significant signs of pitting or degradation. This selective corrosion behavior underscores the importance of microstructural uniformity in determining the alloy's overall corrosion resistance. The protective oxides (TiO_2) and niobium pentoxide (Nb_2O_5) act synergistically to safeguard the alloy against further corrosion. The TiO_2, with its high corrosion resistance and biocompatibility, forms a dense and adherent layer that

effectively blocks corrosive agents. Similarly, Nb_2O_5 enhances the stability of the passive film by contributing to the integrity and durability of the protective layer. Together, these oxides create a robust barrier, ensuring that the Ti-xNb alloys maintain their structural and chemical stability even in aggressive environments. The EDS spectra complement the microstructural observations by confirming an increasing Nb content from 4.02 wt.% in Ti-5Nb to 19.91 wt.% in Ti-25Nb. Concurrently, the oxygen content remains moderately high (6.31–9.84 wt.%), suggesting oxide formation; however, the corrosion resistance does not improve proportionally with Nb content.

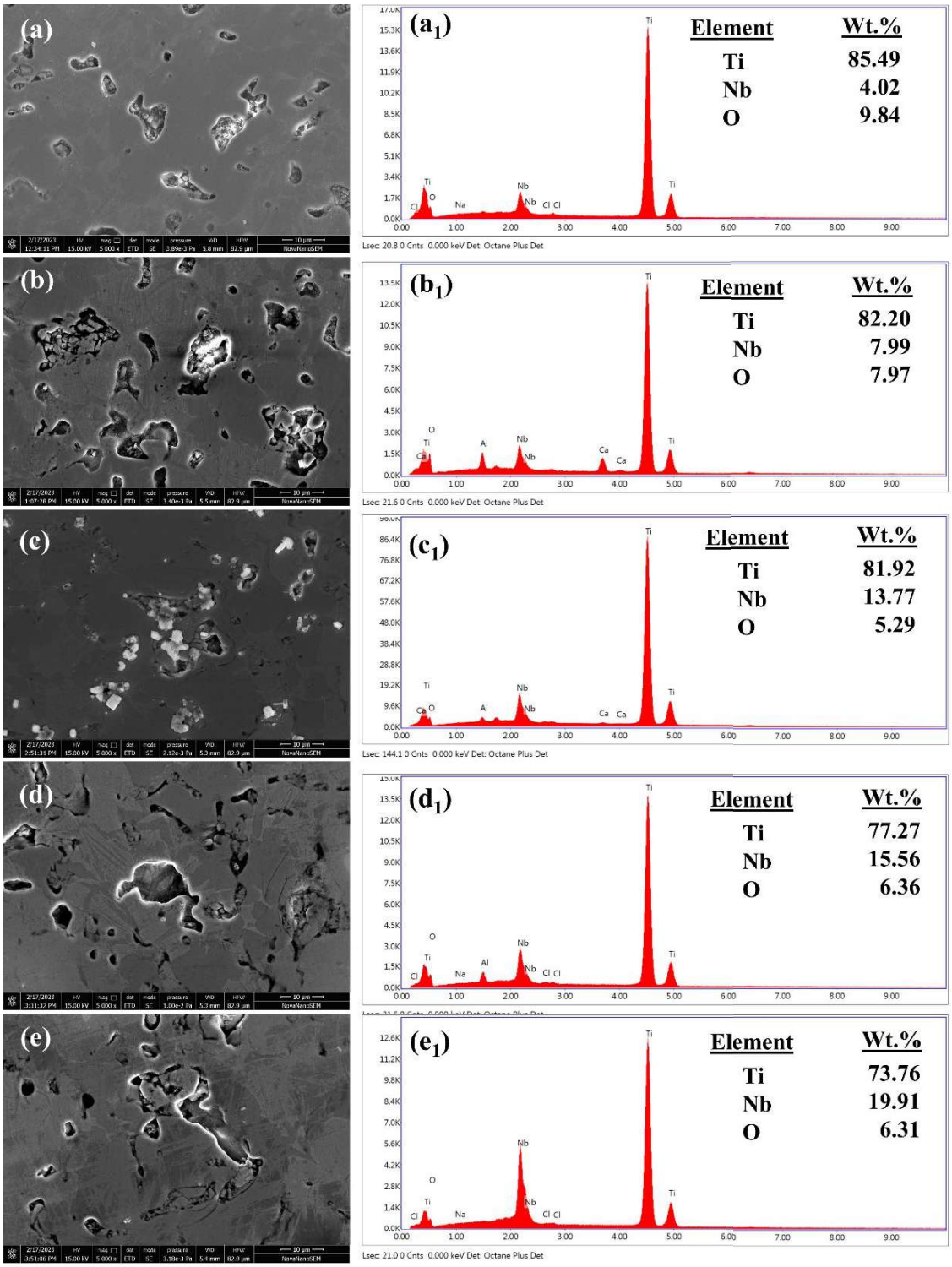

Fig. 5.7: SEM images and EDS analysis of corroded surface of (a) Ti-5Nb, (b) Ti-10Nb, (c) Ti-15Nb, (d) Ti-20Nb, and (e) Ti-25Nb alloys and corresponding EDS spectra in (a_1-e_1)

The SEM images of the corroded surfaces of Ti-xZr alloys, shown in Fig. 5.8, demonstrate their superior corrosion resistance with minimal signs of degradation. Unlike Ti-Nb alloys, Ti-xZr alloys exhibit excellent surface appearance and show only minor corrosion near large pores, with no visible damage around smaller pores. This enhanced resistance is attributed to the formation of a stable and adherent oxide layer of TiO_2 and zirconium dioxide (ZrO_2), which acts as a protective barrier, preventing further corrosion. The synergy between TiO_2 and ZrO_2 significantly enhances the alloys' durability, making them well-suited for demanding applications such as biomedical implants. The corresponding EDS spectra further confirm the surface chemistry, showing a progressive increase in Zr content from 4.02 wt.% in Ti-5Zr to 18.58 wt.% in Ti-20Zr, indicating successful alloying and enhanced oxide film stability. Oxygen content remains relatively low, suggesting the formation of a thin yet protective passive layer. The synergy between TiO_2 and ZrO_2 contributes to improved passivation behavior, reinforcing the chemical stability and surface protection of the alloys.

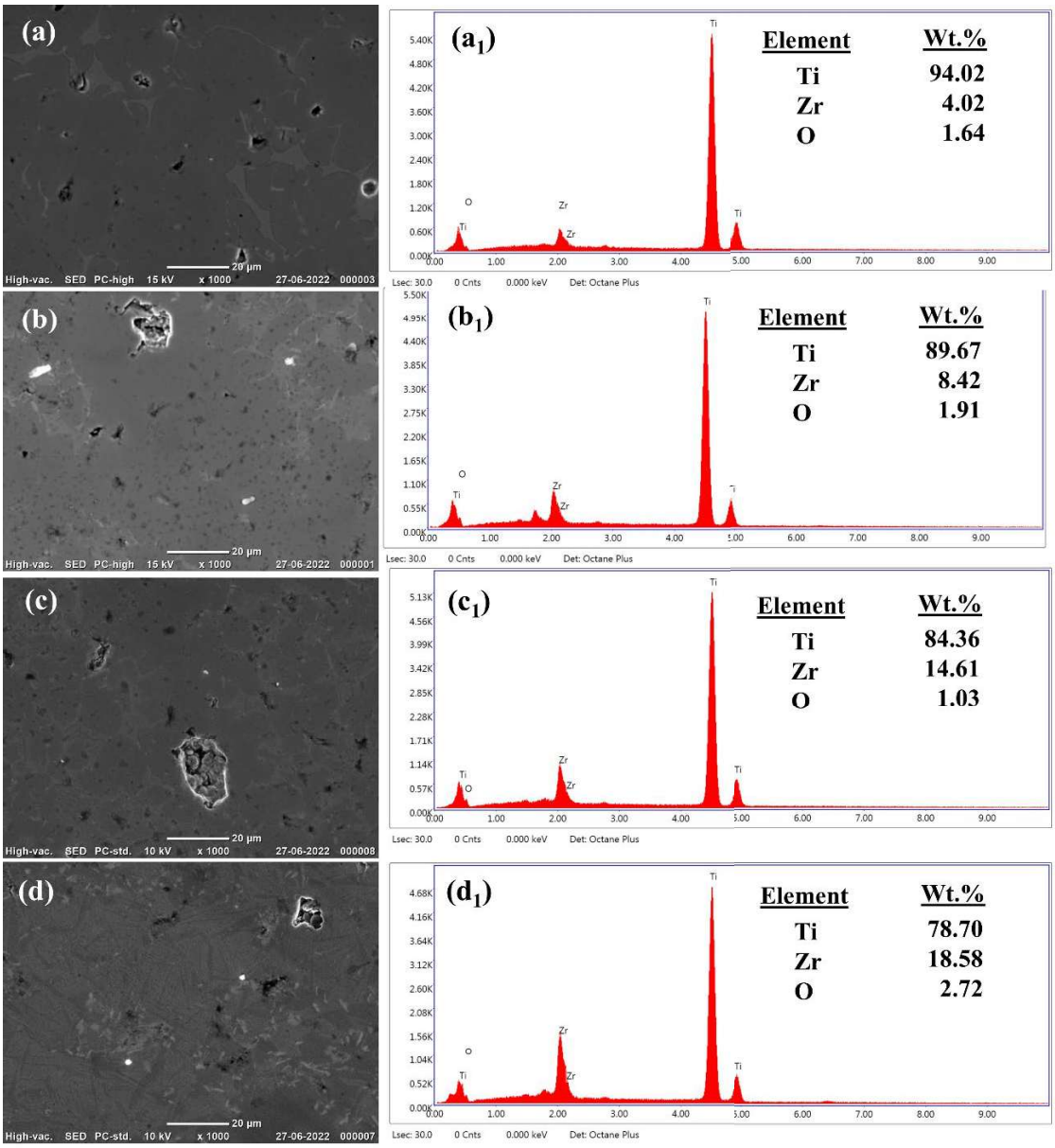

Fig. 5.8: SEM images and EDS analysis of corroded surface of (a) Ti-5Zr, (b) Ti-10Zr, (c) Ti-15Zr, and (d) Ti-20Zr alloys and corresponding EDS spectra in (a_1-e_1)

The SEM images of Ti-10Zr-xNb alloys after corrosion, shown in Fig. 5.9, reveal significant corrosion damage compared to Ti-Nb and Ti-Zr alloys. A large portion of the surface is severely affected by corrosion. This increased corrosion can be attributed to the compaction pressure and porosity of the samples. The Ti-10Zr-xNb alloys were compacted at 600 MPa instead of 650 MPa, resulting in porosity levels exceeding 25% in all the alloys. While this lower compaction pressure was chosen to reduce the elastic modulus, which met the design objective, it inadvertently increased the corrosion rate. The higher porosity leads to a larger surface area, which is advantageous for biocompatibility and promoting bone growth on the implant. However, the increased surface area and reduced density also make the alloys more susceptible to corrosion. The corresponding EDS spectra validate the compositional trend, confirming rising Nb content from 4.64 wt.% in Ti-10Zr-5Nb to 21.48 wt.% in Ti-10Zr-20Nb, while Zr content remains nearly constant across the samples. The oxygen content across the alloy ranges between 2.72 and 3.41 wt.%, confirming oxide formation on the surface. However, despite oxide presence, the corrosion resistance did not improve with Nb addition, likely due to the formation of a less stable and more defective β-phase oxide film at higher Nb levels.

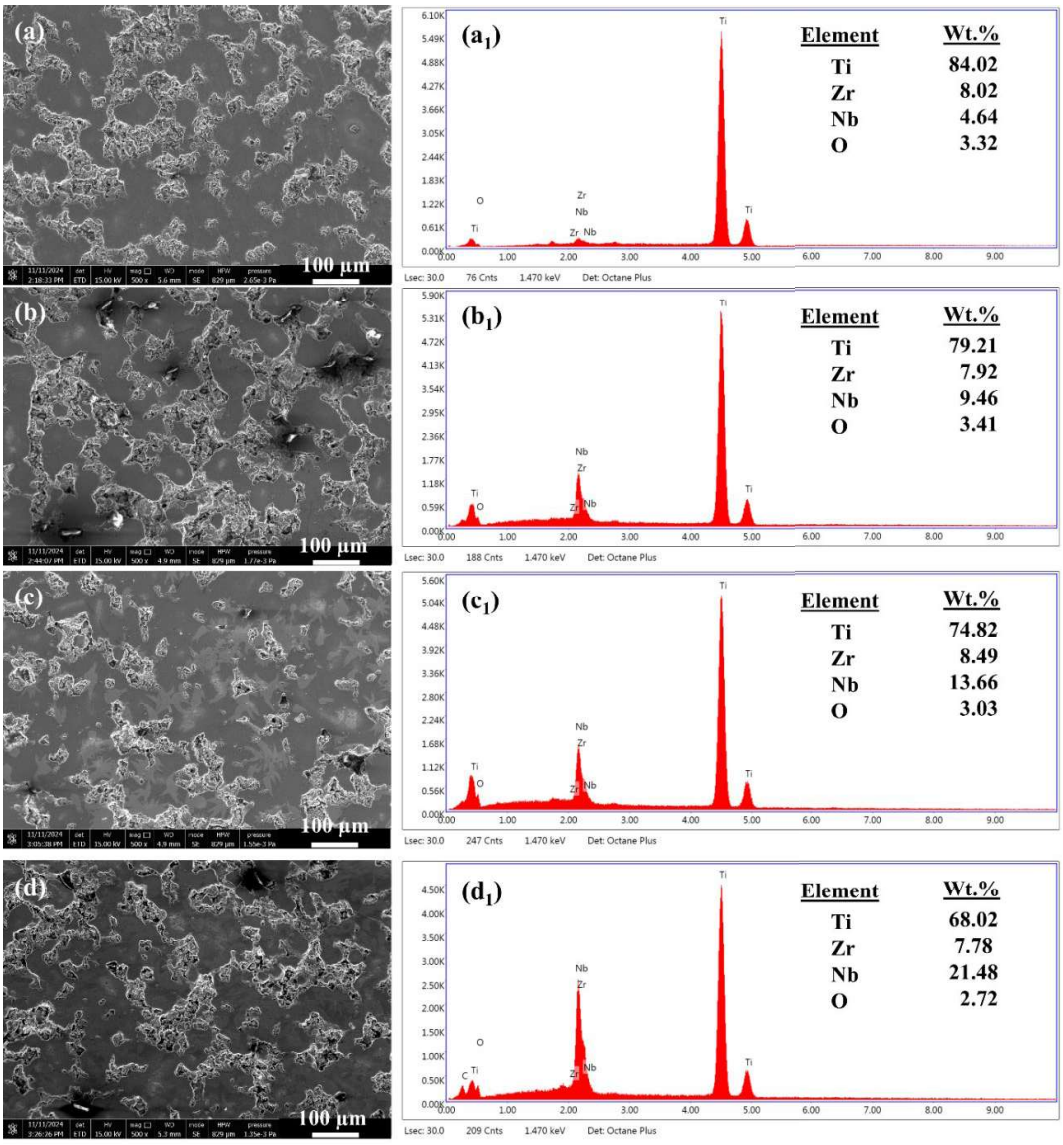

Fig. 5.9: SEM images and EDS analysis of corroded surface of (a) Ti-10Zr-5Nb, (b) Ti-10Zr-10Nb, (c) Ti-10Zr-15Nb, and (d) Ti-10Zr-20Nb alloys and corresponding EDS spectra in (a_1-d_1)

The high entropy is a special class of material, which is in trends now a days and known for its excellent mechanical properties. Both of the high entropy alloys subjected to corrosion have been analyzed for their corroded surfaces. The SEM images of corroded surface of $TiNb_{1.5}Mo_{1.1}Zr_{1.15}Cu_{0.25}$ and $TiNbZr_{0.8}Mo_{0.92}Sn_{0.28}$ HEA shown in Fig 5.10. The corrosion of HEA Cu resulted into the chemical degradation and the visible marks

of corrosion can be observed in Fig. 5.10(a) along with adhered product of corrosion. While the HEA Sn has less corrosion and similar to binary and ternary alloys, the oxides have been observed near the pores areas. While the other areas show better resistance against the corrosion. The EDS spectra support the morphological observations. For the Cu-containing HEA, the presence of 3.33 wt.% oxygen and 4.23 wt.% copper, along with high Ti (23.68 wt.%) and Mo (24.55 wt.%) content, suggests partial passivation, although Cu may locally disrupt passive film stability. Conversely, the Sn-containing HEA shows increased oxygen content (7.33 wt.%), implying higher oxide formation due to aggressive corrosion. Notably, the Ti content drops to 15.67 wt.% while Nb and Mo remain high (30.83 wt.% and 25.37 wt.%, respectively), which may contribute to the formation of unstable mixed oxides.

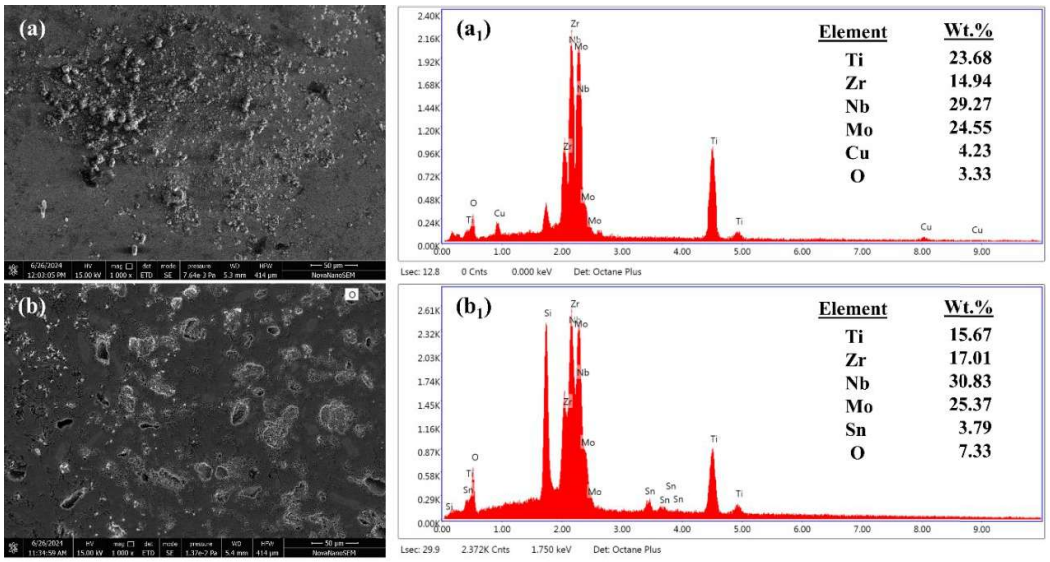

Fig. 5.10: SEM images and EDS analysis of corroded surface of (a) sintered $TiNb_{1.5}Mo_{1.1}Zr_{1.15}Cu_{0.25}$ HEA, (b) sintered $TiNbZr_{0.8}Mo_{0.92}Sn_{0.28}$ HEA

5.2 Tribological behaviour

5.2.1 Frictional behaviour

5.2.1.1 Frictional behaviour of cpTi and Ti-6Al-4V

Figure 5.11 and 5.12 shows the coefficient of friction response of cpTi and Ti-6Al-4V. The friction response with respect to cycle for cpTi is shown in Fig. 5.11. The friction response at lower load is fluctuating kind, while more stable kind of response can be observed at higher load of 40 N. This fluctuation may be related to the continuous breaking of surface layer and exposed to new smooth layer. During the breaking of rough layer friction is higher and with smooth new layer friction is lower. This trend is repetitive throughout complete test cycle. Unlike the trend of cpTi and Ti-6Al-4V have very close friction response at all four loads. This alloy shows stable kind of friction response as compared to cpTi. However, as the cycle progresses, the response of friction becomes fluctuating at higher loads.

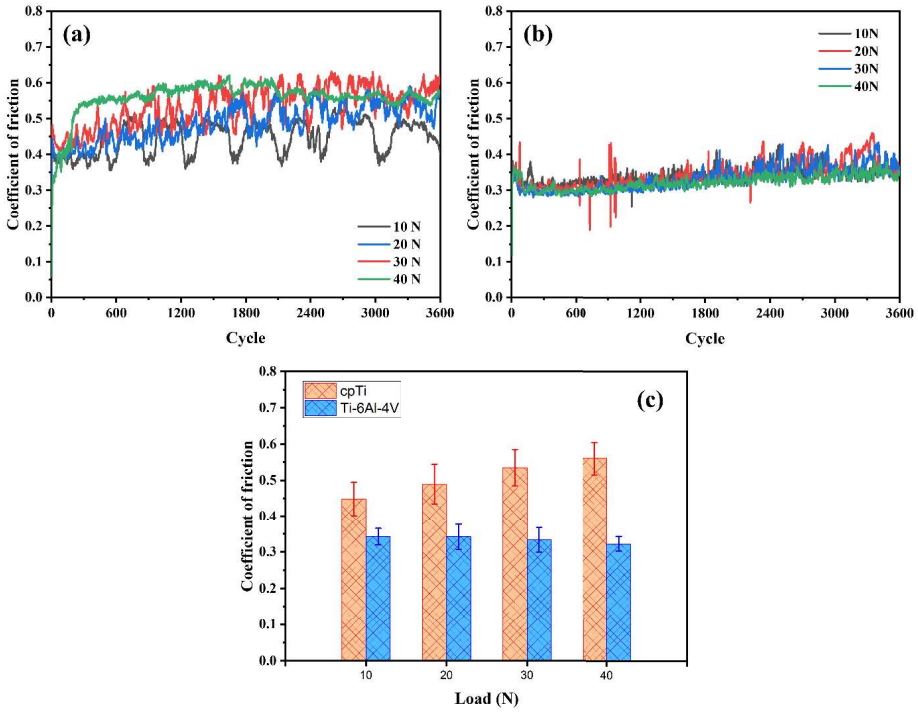

Fig. 5.11: Coefficient of friction response for (a) cpTi, (b) Ti-6Al-4V, (c) average friction coefficient of cpTi and Ti-6Al-4V

5.2.1.2 Frictional behaviour of sintered binary alloys

The variation of the coefficient of friction (COF) with respect to cycles under SBF condition is shown in Fig. 5.12. The Ti-Nb alloys exhibit the decreasing trend in COF with increasing cycles, indicating stable tribological behavior in SBF. The friction response shows a characteristic fluctuating pattern, suggesting that a surface layer intermittently offers resistance for a certain number of cycles. During this phase, the upper counter face repeatedly interacts with the asperities of the lower disc sample, eventually breaking the surface layer after repeated impacts. This leads to a temporary reduction in COF due to uneven asperity contact resulting from surface wear. After a few cycles, proper engagement is reestablished with the counter face, and the cycle of resistance and breakdown repeats. This periodic pattern of peaks and valleys is consistently observed throughout the test. The average COF values for the Ti-Nb alloys are calculated and presented in the graph. The results indicate that the incorporation of Nb enhances the antifriction behavior, with the most significant improvement observed up to 10% Nb addition. Beyond this concentration, a moderate increase in COF is noted; however, the values remain favorable for tribological applications. These findings confirm that the presence of Nb contributes to improved frictional performance of Ti-Nb alloys in SBF conditions.

For all developed alloys, the coefficient of friction (COF) changes as a function of cycle as shown in Fig. 5.12. The experiment consisted of 3600 cycles because the reciprocation was performed at 1 Hz frequency for 1 hour. Initially, all alloys demonstrate an increase in COF, followed by a subsequent decline after a certain number of cycles. This behavior can be reasonably attributed to the early cycles, during which the tribo pairs exhibit a higher degree of sharp asperity contacts. Subsequently, as cycles progress, these sharp asperities begin to wear and break, leading to a smoother

surface and a reduction in COF values.

Among the various alloys, Ti-5Zr consistently exhibits the highest COF, with a noticeable drop occurring between 1000 and 2200 cycles. In contrast, the lowest COF values observed throughout the cycles belong to Ti-15Zr alloy. Figure 5.12(f) illustrates the average COF values for all alloys, revealing that COF values for all samples fall within the range of 0.2 to 0.3. The addition of Zr serves to lower the COF, with the Ti-15Zr alloy exhibiting the lowest (COF = 0.222) and the Ti-20Zr alloy registering the highest (COF = 0.298). Consequently, the frictional force experienced by the Ti-15Zr alloy is the lowest among all the developed alloys. The introduction of Zr contributes to increase the hardness, thereby enhancing the frictional resistance of the alloy [227].

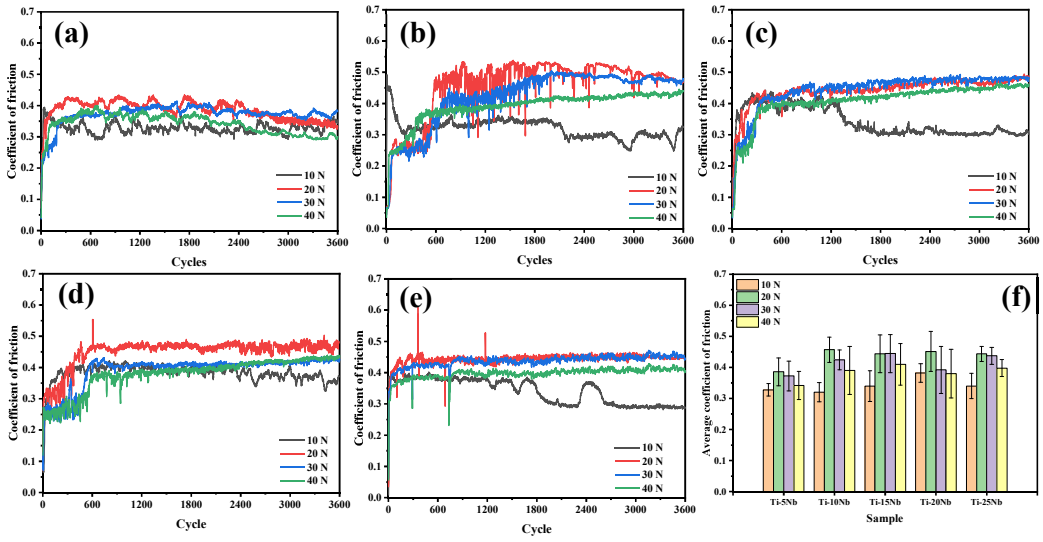

Fig. 5.12: Coefficient of friction of Ti-xNb alloys in SBF (a) Ti-5Nb, (b) Ti-10Nb, (c) Ti-15Nb, (d) Ti-20Nb, (e) Ti-25Nb, and (f) Average COF response

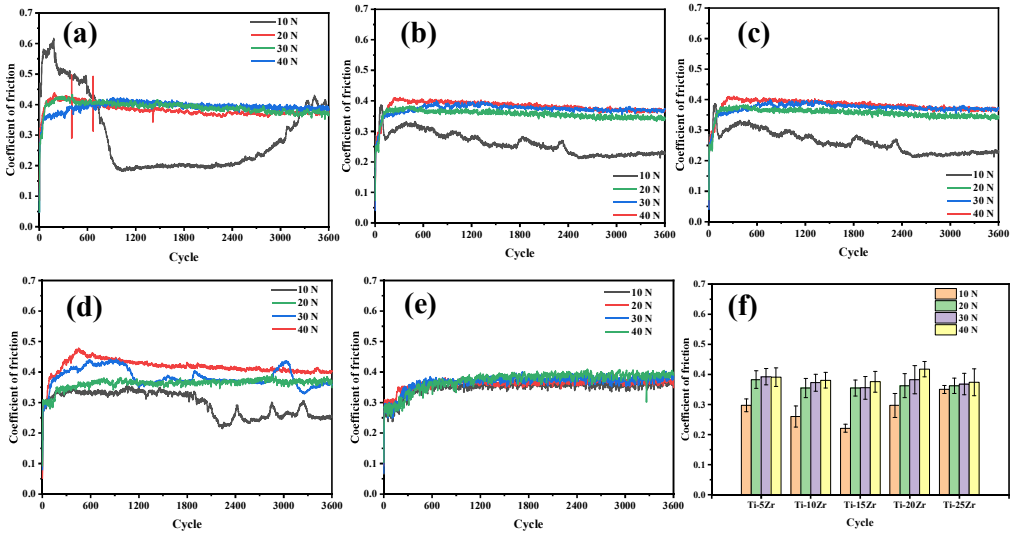

Fig. 5.13: Coefficient of friction of Ti-xZr alloys in SBF (a) Ti-5Zr, (b) Ti-10Zr, (c) Ti-15Zr, (d) Ti-20Zr, (e) Ti-25Zr, and (f) Average COF response

5.2.1.3 Frictional behaviour of sintered ternary alloys

The frictional response of Ti-10Zr-xNb alloys is shown in Fig. 5.14. The coefficient of friction in all these ternary alloys are comparatively higher than the binary alloys. This higher friction in ternary alloys is mainly attributed to its higher level of porosity. The higher porosity in the sample results into more interlocking of the asperities with counter hard surface, which increased the friction coefficient of the friction pair. The friction coefficient is increasing with Nb content, which justify the above-mentioned reason of increased porosity level. In Ti-10Zr-5Nb and Ti-10Zr-10Nb friction is increasing with the increasing loads. However, in Ti-10Zr-15Nb and Ti-10Zr-20Nb opposite trends have been observed. With the increasing load from 20 to 40 N the friction is reducing slightly. This reduction may be obtained due to the increased Nb content reduce the hardness and increased the wear. These wear debris are become sacrificial between asperities and act as an intermediate layer to reduce the friction between the friction pair.

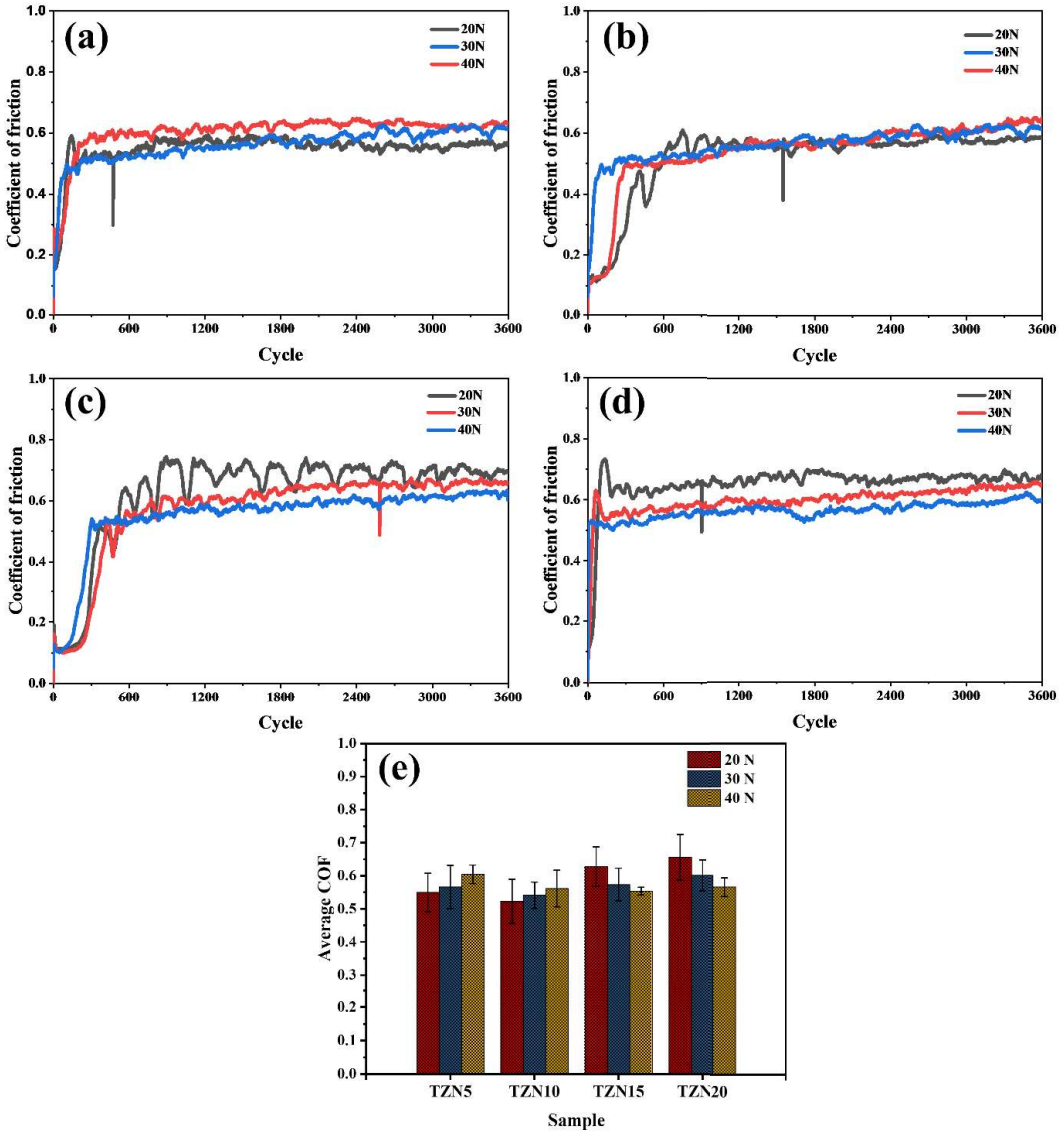

Fig. 5.14: Coefficient of friction of Ti-10Zr-xNb alloys in SBF (a) Ti-10Zr-5Nb, (b) Ti-10Zr-10Nb, (c) Ti-10Zr-15Nb, (d) Ti-10Zr-20Nb, (e) Average COF response

5.2.1.4 Frictional behaviour of sintered high entropy alloys

Figure 5.15 shows, initial COF value is very low, but it increases over time, this is because initially the sample surface is very smooth due to polishing, and once the upper surface wears out, the COF value rises significantly. In another part, we can see that the COF value decreases after a certain number of cycles. This is because the worn particles from the surface act as a lubricant, which helps to reduce the COF value.

Figure 5.15(c) bar diagram shows the average value of COF of both the HEAs. For $TiNb_{1.5}Mo_{1.1}Zr_{1.15}Cu_{0.25}$ at 20N COF is 0.47306 and at 30N is 0.49017. Similarly, for $TiNbZr_{0.8}Mo_{0.92}Sn_{0.28}$ COF at 20N is 0.36783 and at 30N is 0.38728. This indicates that the COF value is slightly higher under increased loading conditions compared to lower loads.

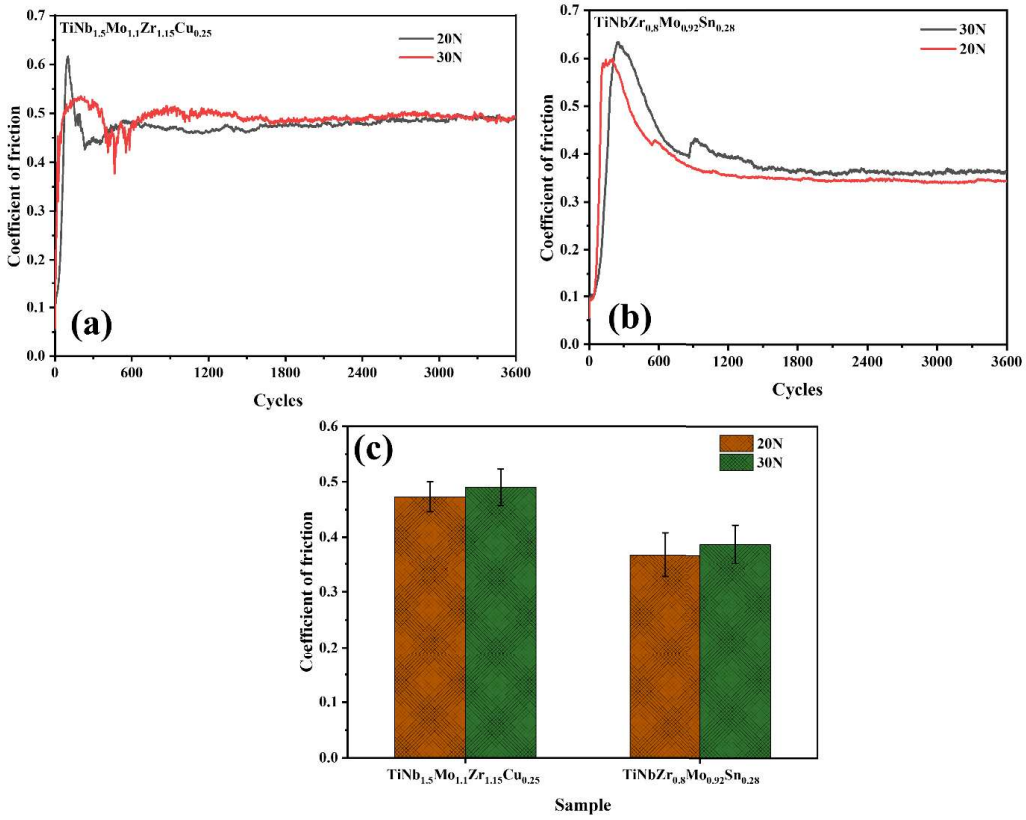

Fig. 5.15: COF vs Cycle graph of (a) $TiNb_{1.5}Mo_{1.1}Zr_{1.15}Cu_{0.25}$ HEA, (b) $TiNbZr_{0.8}Mo_{0.92}Sn_{0.28}$ HEA and (c) Average COF response

5.2.2 Wear behaviour

5.2.2.1 Wear behaviour of cpTi and Ti-6Al-4V

The wear tracks at four loads measured through profilometer for cpTi and Ti-6Al-4V are shown in Fig. 5.16 and Fig. 5.17, respectively. The track depth increases with increasing loads from 10 to 40 N. Similar to track depth, track width also increases with the normal load. The area of these profiles is measured through Origin software are given in Table 5.11 and 5.12, respectively. With the help of these track width and track area, the wear volume and wear rates determined from the formula given in Eqs. (3.9) and (3.10) are given in Table 5.11 and 5.12. The wear volume of cpTi is lowest at 0.103 mm^3 under a 10 N load, while it increases up to 0.606 mm^3 at 40 N load. Furthermore, the results presented in Table 5.12 show the wear behavior of Ti-6Al-4V at different applied loads (10 N, 20 N, 30 N, and 40 N) in SBF conditions. The wear behavior of Ti-6Al-4V shows that the wear scar width, cross-sectional area, and wear volume all increases with applied load, indicating higher stress and greater material loss at higher loads.

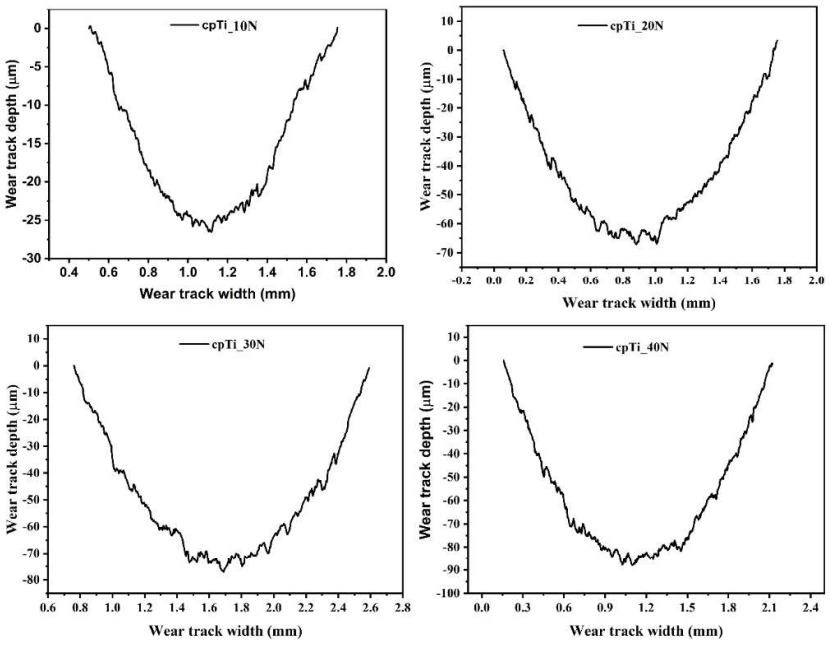

Fig. 5.16: Wear track profile of cpTi at 10, 20, 30, and 40 N loads

Table 5.11: Wear scar parameters, wear volume, and wear rates of cpTi at 10, 20, 30, and 40 N in SBF condition

Load	wear scar width W (μm)	Wear scar cross-sectional area Aw ($μm^2$)	Wear volume (mm^3)
10	1249.636	19723.74	0.103
20	1696.855	74486.34	0.403
30	1830.113	89235.77	0.483
40	1964.769	111112.49	0.606

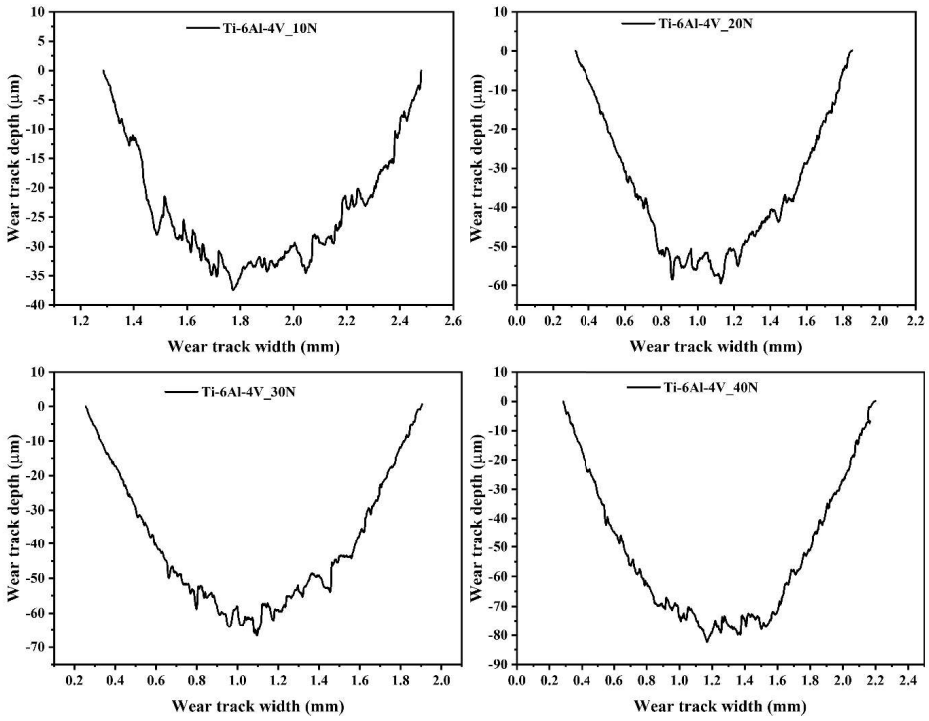

Fig. 5.17: Wear track profile of Ti-6Al-4V at 10, 20, 30, and 40 N loads

Table 5.12: Wear scar parameters, wear volume, and wear rates of Ti-6Al-4V at 10, 20, 30, and 40 N in SBF condition

Load	wear scar width W (µm)	Wear scar cross-sectional area Aw (µm^2)	Wear volume (mm^3)
10	1194.819	28614.07	0.152
20	1525.415	54413.08	0.292
30	1689.908	66515.01	0.357
40	1916.016	99651.42	0.541

5.2.2.2 Wear behaviour of sintered binary alloys

The wear performance of the Ti-Nb samples was assessed by determining their wear volume and wear rate using Equations (3.9) and (3.10). A profilometer was used to obtain the wear track profiles, from which the average depth and cross-sectional area were computed using Origin software. Figures 5.18 to 5.21 display the wear track profiles for the various Ti-Nb alloys, and the corresponding parameters are detailed in Tables 5.13 to 5.16. By substituting the values of $\bar{A}_w$, $\bar{D}$, R, l, and S in Eqs. (3.9) and (3.10), the wear volume and wear rates were calculated and included in the same tables. From Figs. 5.18 to 5.21, the minimum wear track depth under SBF condition is observed for the Ti-10Nb alloy, measuring approximately 15 microns. For the other Ti-Nb alloys, the wear track depth ranges between 10 and 18 microns, which is slightly higher than Ti-10Nb. Correspondingly, Ti-10Nb also exhibits the smallest wear track area, as confirmed by the data in Tables 5.13 to 5.16. Although the wear track area for the other Ti-Nb alloys is larger, it remains within a relatively low range. As a result, the Ti-10Nb alloy demonstrates the lowest wear volume and wear rate among all Ti-Nb compositions. The alloys with Nb content above 10% show a slight increase in wear volume and wear rate compared to Ti-10Nb, but still exhibit favorable antiwear

performance. These results suggest that Nb addition significantly enhances the wear resistance of Ti-Nb alloys in SBF, with optimal performance observed at 10% Nb.

Figure 5.22 to Fig. 5.25 shows the wear scar profile of all developed Ti-xZr alloys obtained by the profilometer. Wear scar depth for the Ti-15Zr alloy is lowest among all the developed alloys while the maximum depth is obtained for Ti-10Zr alloy. The wear rate and wear volumes for all the developed alloys is shown in Table 5.17 to 5.20. It is evident that as the Zr component in the developed alloys increases, wear volume and wear rate decrease, except for Ti-10Zr which has the highest wear track width, wear rate, and wear volume. However, it exhibits comparatively lower volume loss and lower wear rate compared to SS 316L, cpTi, and Ti-6Al-4V alloy [228]. The addition of Zr improves the mechanical and physical properties of the alloys, which further helps to improve their tribological performance [195,229]. The density and hardness have also increased in this study with the addition of Zr, and the antifriction and antiwear behavior is in accordance with the hardness. Although despite having highest hardness of Ti-10Zr the wear volume is highest among all developed alloys. This may be due to higher oxygen absorbing capacity might have induced brittleness in this alloy resulting in the highest wear rate [195]. In addition, the wear track width, depth, and wear volume increasing with the loads. The higher loads apply more stress at the contacting surfaces results into more plastic deformation and fracture of surfaces than at lower loads.

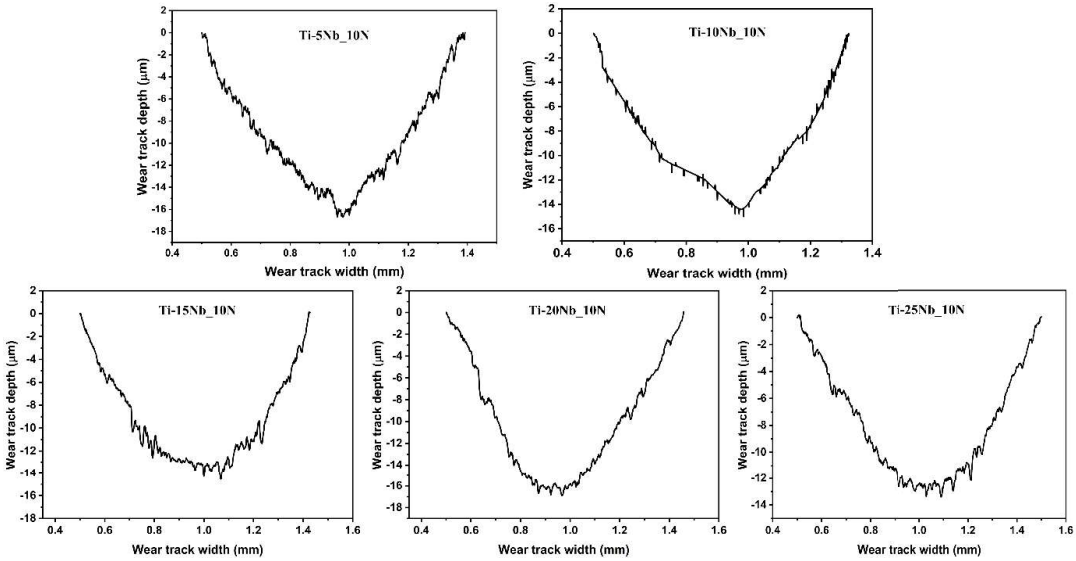

Fig. 5.18: Wear track profile of Ti-xNb alloys at 10 N

Table 5.13: Wear scar parameters, wear volume, and wear rates of Ti-xNb alloys at 10 N in SBF condition

Samples	wear scar width W (μm)	Wear scar cross-sectional area A_w (μm^2)	Wear volume (mm^3)
Ti-5Nb	915.35	8369.36	0.043
Ti-10Nb	860.25	7341.27	0.038
Ti-15Nb	923.23	8530.85	0.044
Ti-20Nb	957.22	9463.05	0.049
Ti-25Nb	895.71	7899.59	0.041

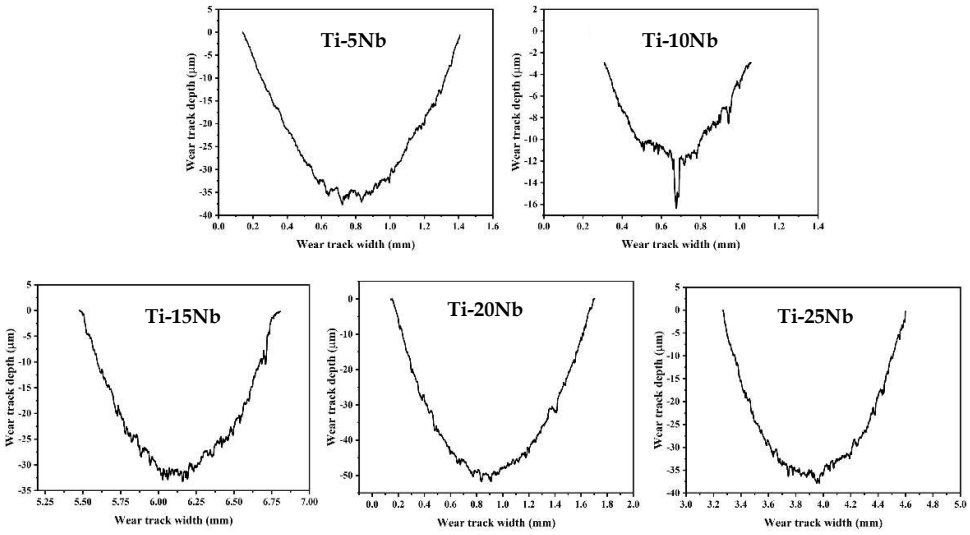

Fig. 5.19: Wear track profile of Ti-xNb alloys at 20 N

Table 5.14: Wear scar parameters, wear volume, and wear rates of Ti-xNb alloys at 20 N load in SBF condition

Samples	wear scar width W (μm)	Wear scar cross-sectional area Aw (μm^2)	Wear volume (mm^3)
Ti-5Nb	1268.259	29114.108	0.154
Ti-10Nb	961.735	7747.460	0.045
Ti-15Nb	1329.448	27319.605	0.143
Ti-20Nb	1563.591	51765.449	0.276
Ti-25Nb	1331.721	33282.839	0.176

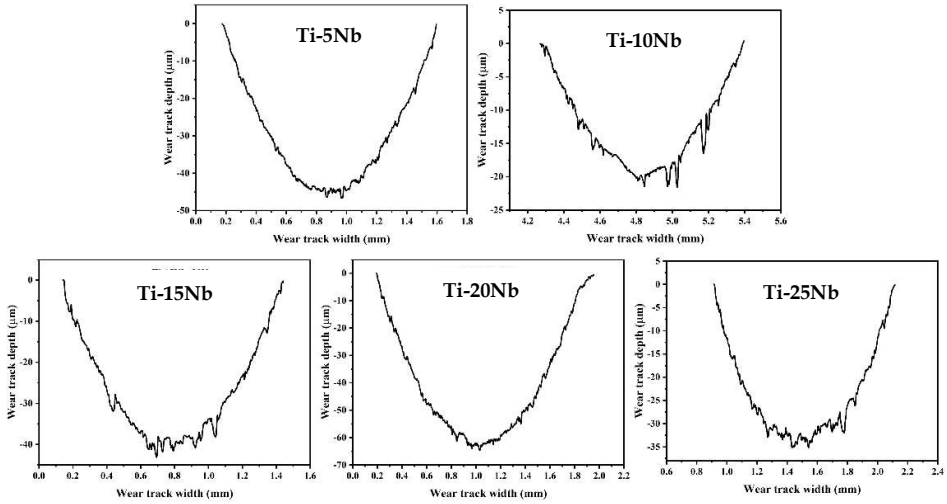

Fig. 5.20: Wear track profile of Ti-xNb alloys at 30 N

Table 5.15: Wear scar parameters, wear volume, and wear rates of Ti-xNb alloys at 30 N load in SBF condition

Samples	wear scar width W (μm)	Wear scar cross-sectional area Aw (μm^2)	Wear volume (mm^3)
Ti-5Nb	1421.169	42271.572	0.225
Ti-10Nb	1127.115	14472.678	0.074
Ti-15Nb	1298.951	34862.129	0.185
Ti-20Nb	1744.601	69693.227	0.373
Ti-25Nb	1200.745	28233.199	0.149

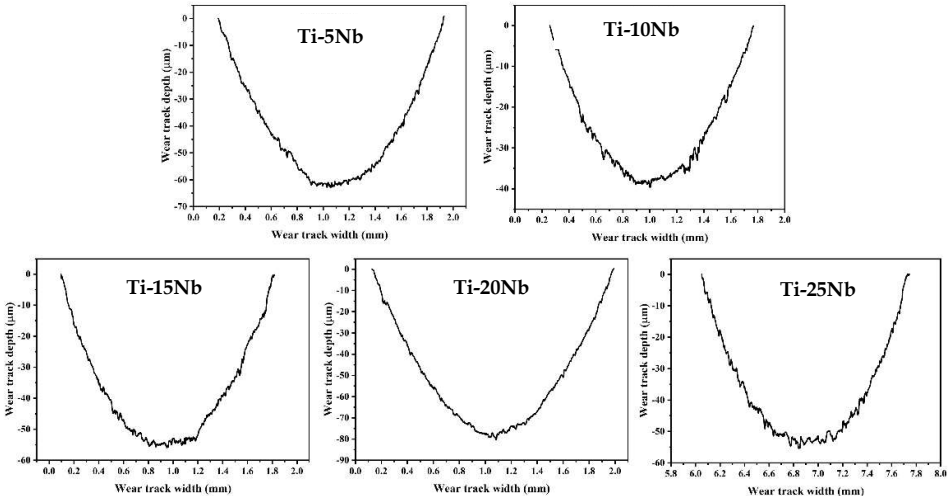

Fig. 5.21: Wear track profile of Ti-xNb alloys at 40 N

Table 5.16: Wear scar parameters, wear volume, and wear rates of Ti-xNb alloys at 40 N load in SBF condition

Samples	wear scar width W (μm)	Wear scar cross-sectional area A_w (μm^2)	Wear volume (mm^3)
Ti-5Nb	1735.486	72470.554	0.389
Ti-10Nb	1511.035	38811.606	0.204
Ti-15Nb	1712.937	64364.044	0.343
Ti-20Nb	1862.108	94163.120	0.510
Ti-25Nb	1684.014	62659.863	0.334

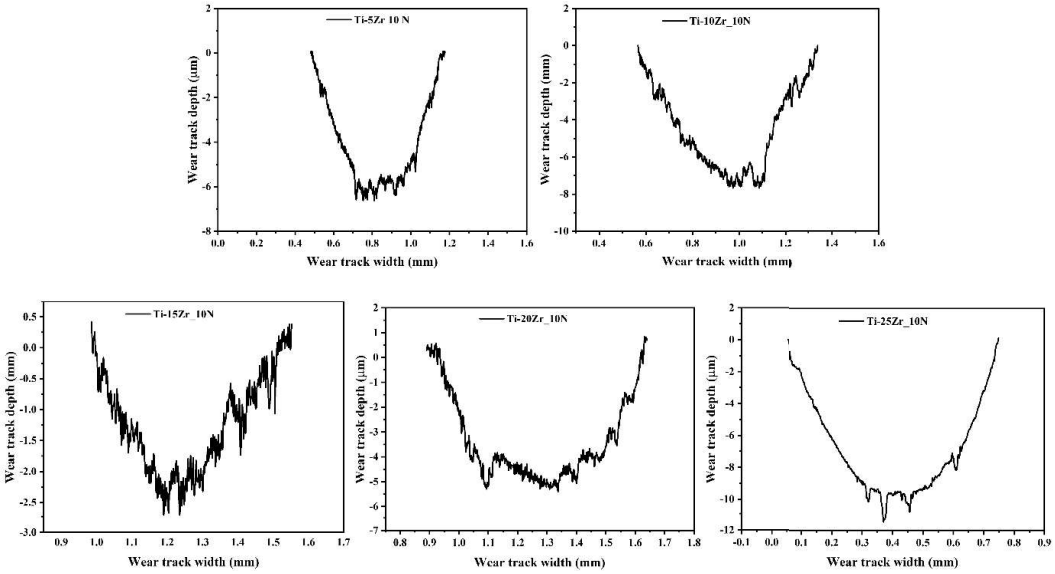

Fig. 5.22: Wear track profile of Ti-xZr alloys at 10 N

Table 5.17: Cross-sectional area, average wear depth, width of wear scar, wear rate and wear volume of Ti-xZr alloys at 10 N

Samples	Wear scar cross-sectional area A_w (μm^2)	Width of wear scar W (μm)	Wear volume (mm^3)
Ti-5Zr	2774.73	690.22	0.0141
Ti-10Zr	3222.74	745.71	0.0164
Ti-15Zr	878.17	485.23	0.0044
Ti-20Zr	2372.16	660.35	0.0121
Ti-25Zr	2934.15	697.55	0.0175

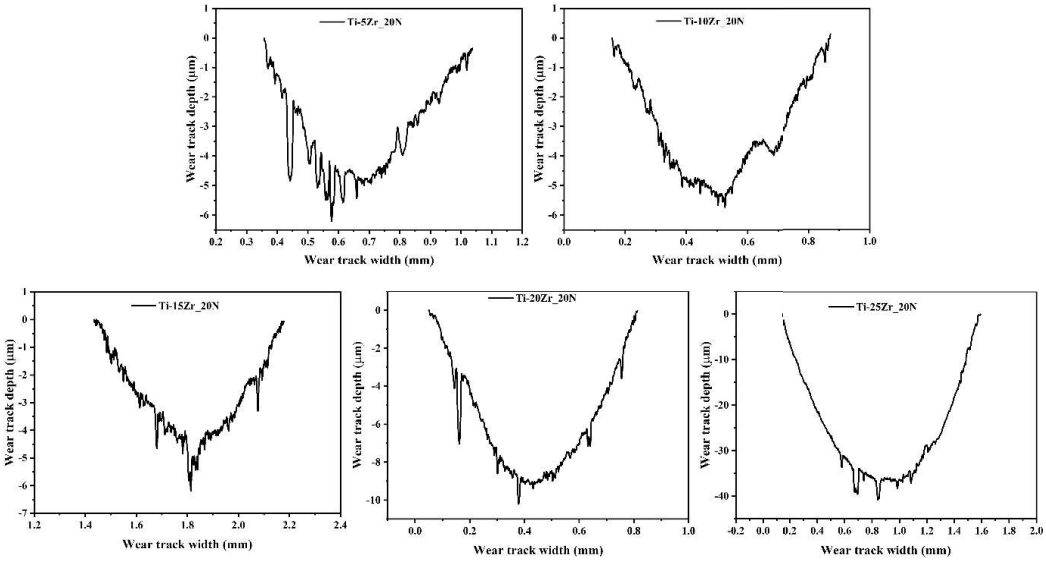

Fig. 5.23: Wear track profile of Ti-xZr alloys at 20 N

Table 5.18: Cross-sectional area, average wear depth, width of wear scar, wear rate and wear volume of Ti-xZr alloys at 20 N

Samples	Wear scar cross-sectional area A_w (μm^2)	Width of wear scar W (μm)	Wear volume (mm^3)
Ti-5Zr	2023.14	680.61	0.0102
Ti-10Zr	2296.77	715.71	0.0116
Ti-15Zr	1869.63	674.05	0.0084
Ti-20Zr	4337.54	763.67	0.0221
Ti-25Zr	36363.24	1431.83	0.1919

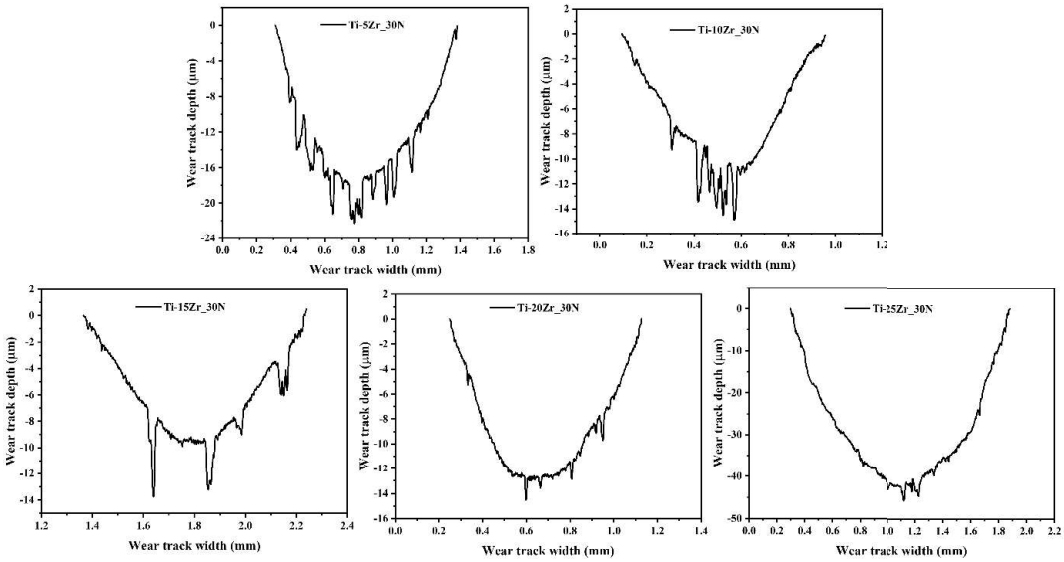

Fig. 5.24: Wear track profile of Ti-xZr alloys at 30 N

Table 5.19: Cross-sectional area, average wear depth, width of wear scar, wear rate and wear volume of Ti-xZr alloys at 30 N

Samples	Wear scar cross-sectional area A_w (µm^2)	Width of wear scar W (µm)	Wear volume (mm^3)
Ti-5Zr	5816.91	864.152	0.0297
Ti-10Zr	13783.19	1069.719	0.0715
Ti-15Zr	5638.4	875.543	0.0288
Ti-20Zr	7644.91	877.129	0.0394
Ti-25Zr	45728.21	1583.806	0.2417

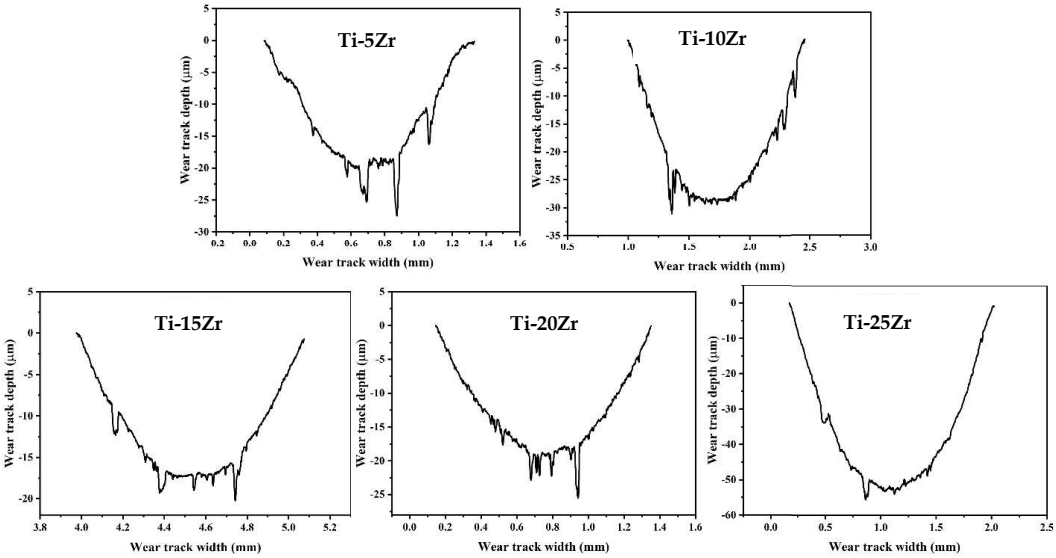

Fig. 5.25: Wear track profile of Ti-xZr alloys at 40 N

Table 5.20: Cross-sectional area, average wear depth, width of wear scar, wear rate and wear volume of Ti-xZr alloys at 40 N

Samples	Wear scar cross-sectional area A_w (μm^2)	Width of wear scar W (μm)	Wear volume (mm^3)
Ti-5Zr	15224.43	1245.008	0.0784
Ti-10Zr	64924.61	1847.691	0.3439
Ti-15Zr	8799.45	1123.23	0.0435
Ti-20Zr	15428.78	1205.491	0.0797
Ti-25Zr	28661.62	1465.147	0.1493

5.2.2.3 Wear behaviour of sintered ternary alloys

The wear behavior of Ti-10Zr-xNb alloys under 20 N to 40 N load shown through wear track profile in Fig. 5.26 to 5.28, reveals variations in wear scar parameters and wear rates depending on the Nb content. The parameters of wear are given in Table 5.21 to 5.23. The Ti-10Zr-5Nb alloy shows a moderate cross-sectional area of the wear scar

(29680.0 μm^2) and a wear rate of 2.27E-07 mm^3/mm of sliding distance. The Ti-10Zr-10Nb alloy exhibits a significantly larger cross-sectional area (48481.9 μm^2) and a higher wear rate of 4.46E-07 mm^3/mm, indicating that the increase in Nb content leads to greater wear and material loss. In contrast, the Ti-10Zr-15Nb alloy shows a much smaller wear scar area (6962.4 μm^2) and a notably low wear rate of 5.83E-08 mm^3/mm, suggesting improved wear resistance. The Ti-10Zr-20Nb alloy, with a cross-sectional area of 13761.3 μm^2, shows a wear rate of 1.15E-07 mm^3/mm, which is higher than Ti-10Zr-15Nb but still lower than Ti-10Zr-10Nb. Overall, the results indicate that increasing Nb content enhances wear resistance up to a certain level (Ti-10Zr-15Nb), after which further increases in Nb lead to higher wear rates (Ti-10Zr-10Nb). This suggests an optimal Nb concentration for achieving the best wear resistance in Ti-10Zr-xNb alloys. Likewise binary alloys these ternary alloys also show more wear volume at higher loads.

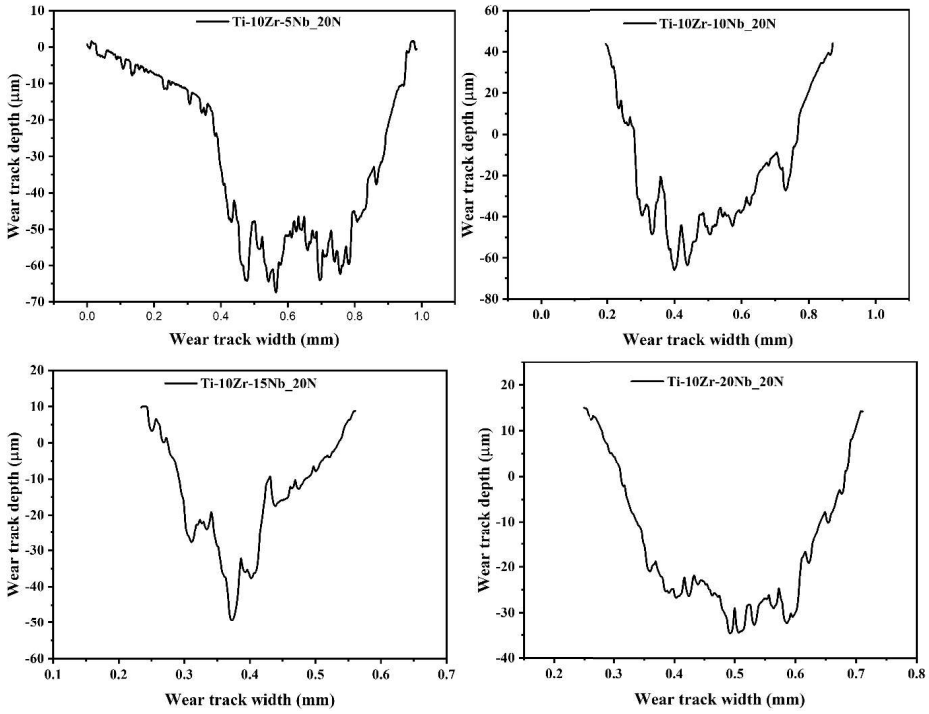

Fig. 5.26: Wear track profile of Ti-10Zr-xNb alloys at 20 N

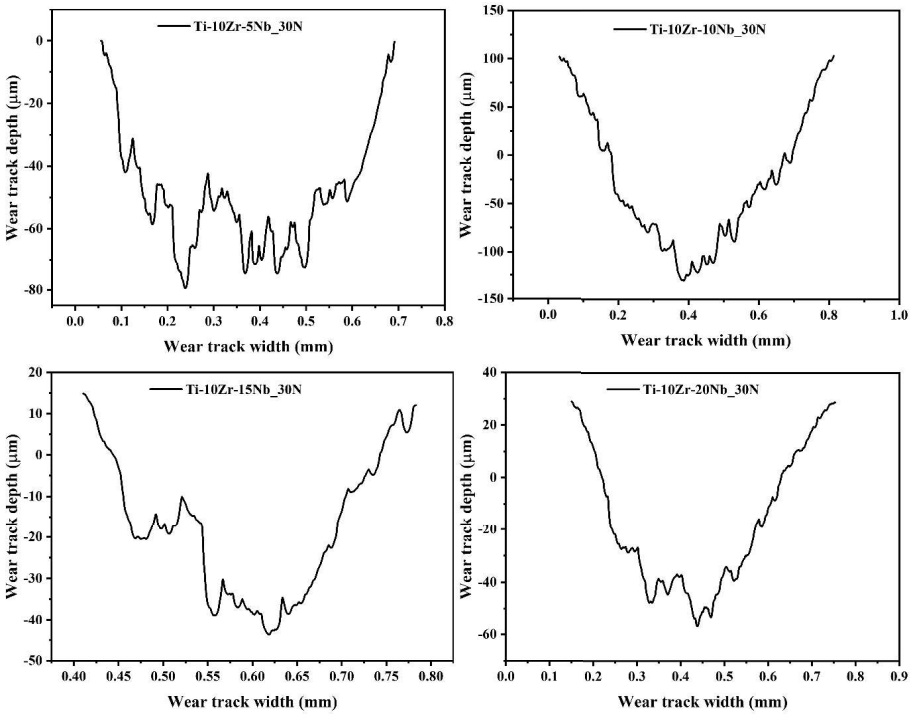

Fig. 5.27: Wear track profile of Ti-10Zr-xNb alloys at 30 N

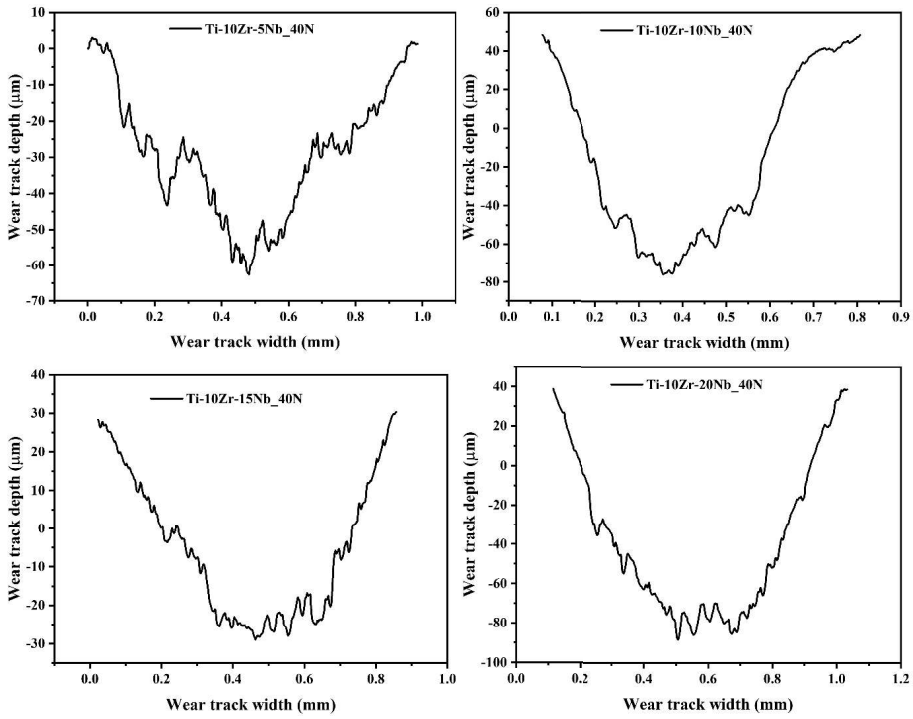

Fig. 5.28: Wear track profile of Ti-10Zr-xNb alloys at 40 N

Table 5.21: Wear parameter of ternary Ti-10Zr-xNb at 20 N

Samples	Wear scar cross-sectional area A_w (μm^2)	Width of wear scar W (μm)	Wear volume (mm^3)
Ti-10Zr-5Nb	29680.0	961.96	0.16
Ti-10Zr-10Nb	48481.9	683.79	0.32
Ti-10Zr-15Nb	6962.4	325.34	0.04
Ti-10Zr-20Nb	13761.3	458.24	0.08

Table 5.22: Wear parameter of ternary Ti-10Zr-xNb at 30 N

Samples	Wear scar cross-sectional area A_w (μm^2)	Width of wear scar W (μm)	Wear volume (mm^3)
Ti-10Zr-5Nb	49491.9	693.79	0.39
Ti-10Zr-10Nb	102910.0	808.56	0.76
Ti-10Zr-15Nb	9848.9	388.92	0.05
Ti-10Zr-20Nb	27519.3	606.15	0.16

Table 5.23: Wear parameter of ternary Ti-10Zr-xNb at 40 N

Samples	Wear scar cross-sectional area A_w (μm^2)	Width of wear scar W (μm)	Wear volume (mm^3)
Ti-10Zr-5Nb	29194.8	839.76	0.19
Ti-10Zr-10Nb	45081.4	733.07	0.28
Ti-10Zr-15Nb	27419.8	835.67	0.15
Ti-10Zr-20Nb	70763.1	907.50	0.44

5.2.2.4 Wear behaviour of sintered high entropy alloys

Figure 5.29 and 5.30 shows the depth and of the wear scar of developed high entropy alloys at different points using profilometer. It can be seen that the wear depth and wear width increase with increase in load. The maximum wear depth is obtained for $TiNb_{1.5}Mo_{1.1}Zr_{1.15}Cu_{0.25}$ at 30N, whereas the minimum depth is obtained for $TiNbZr_{0.8}Mo_{0.92}Sn_{0.28}$ at 20N. From Table 5.24 and Table 5.25, it can be observed that the track width, wear rate and wear volume of $TiNb_{1.5}Mo_{1.1}Zr_{1.15}Cu_{0.25}$ are higher than those of $TiNbZr_{0.8}Mo_{0.92}Sn_{0.28}$ under the same loading conditions. This may be due to the fact that $TiNbZr_{0.8}Mo_{0.92}Sn_{0.28}$ has a higher hardness value than $TiNb_{1.5}Mo_{1.1}Zr_{1.15}Cu_{0.25}$.

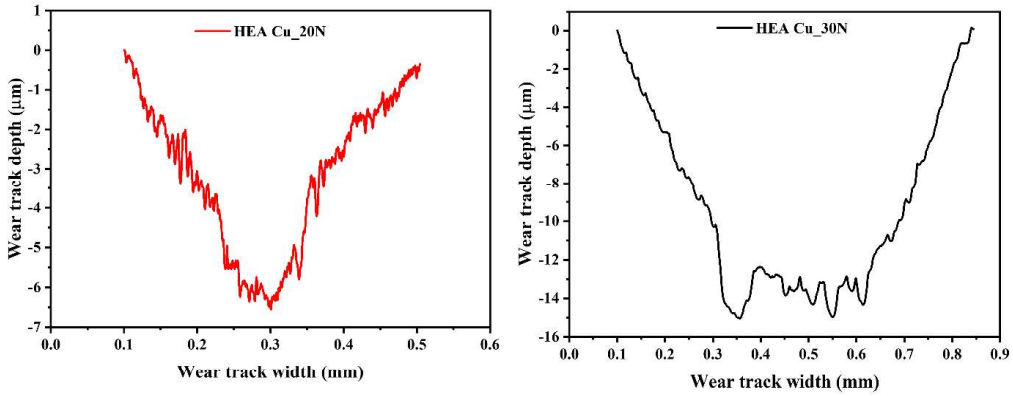

Fig. 5.29: Wear track profile of sintered HEA Cu at 20 and 30 N

Table 5.24: Calculated wear volume and wear rate of sintered HEA Cu at 20 and 30 N

Samples	Load (N)	Wear scar cross-sectional area A_w (µm^2)	Width of wear scar W (µm)	Wear volume (mm^3)
$TiNb_{1.5}Mo_{1.1}Zr_{1.15}Cu_{0.25}$	20	1200.2	403.2	0.0061
$TiNb_{1.5}Mo_{1.1}Zr_{1.15}Cu_{0.25}$	30	6943.5	742.9	0.036088

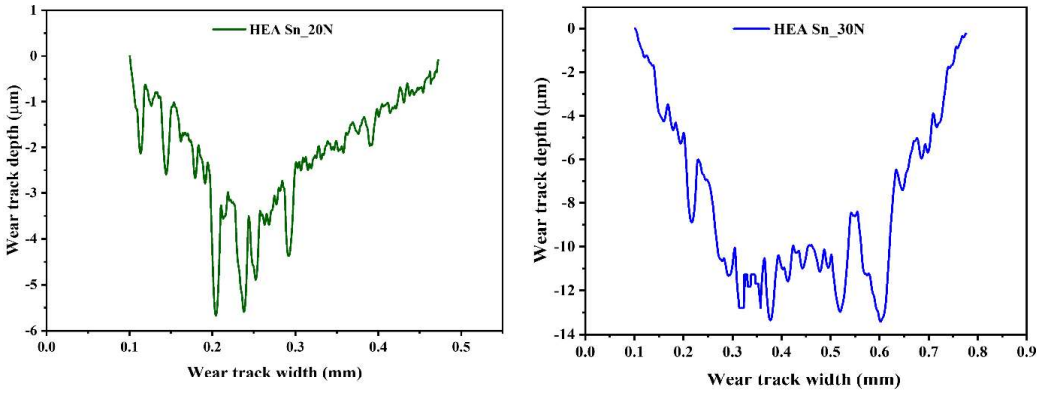

Fig. 5.30: Wear track profile of sintered HEA Sn at 20 and 30 N

Table 5.25: Calculated wear volume and wear rate of sintered HEA Sn at 20 and 30 N

Samples	Load (N)	Wear scar cross-sectional area A_w (μm^2)	Width of wear scar W (μm)	Wear volume (mm^3)
$TiNbZr_{0.8}Mo_{0.92}Sn_{0.28}$	20	787.8	372.8	0.0040
$TiNbZr_{0.8}Mo_{0.92}Sn_{0.28}$	30	5341.5	676.4	0.0277

5.2.3 Worn surface study

The worn surface SEM images of cpTi are shown in Fig. 5.31. The cpTi, being a relatively soft material the Ti-6Al-4V, tends to experience adhesive wear, where material from the titanium surface adhere to the counter face under applied pressure. This results in the transfer of titanium onto the opposing surface, leading to material loss and the formation of wear debris. Additionally, due to its relatively low hardness compared to Ti-6Al-4V, cpTi is more susceptible to abrasive wear. This occurs when harder particles or surfaces come into contact with the titanium surface, leading to material removal through scratching or gouging. On the other hand, similar to cpTi, Ti-6Al-4V can also experience adhesive wear, particularly under high load or poor

lubrication conditions. However, its wear rate is typically lower than cpTi due to its higher hardness and stronger intermetallic bonding between titanium, aluminium, and vanadium.

Other than cpTi and Ti-6Al-4V, both binary alloys Ti-xNb and Ti-xZr experiences dominant abrasive wear along with adhesion mainly at pores and pits regions (Fig. 5.32 to 5.33 and Fig. 5.35 to 5.36). However, the worn surfaces of the ternary alloys Ti-10Zr-xNb, shown in Figs. 5.38 and 5.39, are predominantly characterized by adhesion as the primary wear mechanism. Due to their lower hardness compared to other alloys, their softer surfaces tend to adhere to the counterface, resulting in material removal from the ternary alloys. Moreover, being the hardest materials among all developed alloys, high entropy alloys show dominant oxidative wear rather than abrasion and adhesion mechanism as observed in Fig. 5.39.

Figure 5.34 shows the EDS spectra of worn surfaces of Ti-xNb alloys under a 10 N load, revealing a progressive increase in Nb content from 4.59 wt.% in Ti-5Nb to 23.88 wt.% in Ti-25Nb. This increase corresponds with a decrease in Ti content, indicating compositional consistency across the alloy surface after wear. The worn surface morphology becomes rougher and more fragmented with higher Nb content, suggesting a shift in wear mechanism. At lower Nb levels, the smoother surfaces imply abrasive wear dominance, while at higher Nb levels, the presence of wear debris and surface deformation points to adhesive and oxidative wear mechanisms.

Figure 5.37 illustrates the EDS spectra of worn surfaces of Ti-xZr alloys subjected to a 10 N load, revealing increasing Zr content from 5.22 wt.% in Ti-5Zr to 23.87 wt.% in Ti-25Zr. As Zr concentration rises, the worn surfaces exhibit more prominent wear debris and surface roughness. At lower Zr levels (a-b), the surfaces are relatively smooth, indicative of mild abrasive wear. However, at higher Zr additions (d-e), the

surfaces show increased delamination and debris accumulation, pointing to a transition toward severe adhesive and oxidative wear.

Figure 5.40 shows the EDS spectra and SEM images of worn surfaces of Ti-10Zr-xNb alloys at 20 N, with increasing Nb content from 5.11 wt.% (a_1) to 19.11 wt.% (d_1). All samples retain near-constant Zr content (~8 wt.%), while Ti decreases with Nb addition. Morphologically, the worn surfaces show severe plastic deformation and delamination across all compositions, becoming more pronounced with higher Nb. This suggests a dominant adhesive wear mechanism intensified at elevated Nb levels. The EDS spectra in Figure 5.34 show a gradual increase in Nb content from Ti-5Nb to Ti-25Nb alloys, which correlates with the observed changes in wear mechanisms. At lower Nb content (Ti-5Nb and Ti-10Nb), the worn surfaces exhibit more severe material removal and ploughing marks, suggesting abrasive wear as the dominant mechanism. As the Nb content increases (Ti-15Nb to Ti-25Nb), the surfaces appear smoother with fewer grooves and more protective tribolayers, indicating a transition towards mild adhesive wear. The EDS spectra of worn surfaces for Ti-xZr alloys (Figure) show a gradual increase in Zr content from 5.22 wt.% in Ti-5Zr to 23.87 wt.% in Ti-25Zr. As the Zr content increases, the worn surfaces exhibit reduced material removal and smoother features, indicating a transition from severe abrasive wear to a more stable and protective wear mechanism. The presence of higher Zr likely contributes to improved hardness and wear resistance, resulting in less surface damage under the same testing conditions.

The EDS spectra of worn surfaces for Ti-10Zr-xNb alloys (Figure 5.40) reveal increasing Nb content from 5.11 wt.% to 19.11 wt.%. All compositions exhibit rough and fragmented surfaces, but Ti-10Zr-15Nb shows relatively more compact and continuous tribolayer formation. This indicates a localized shift in wear mechanism

from severe abrasive wear to a more stable delamination-dominated wear only at the 15 wt.% Nb composition.

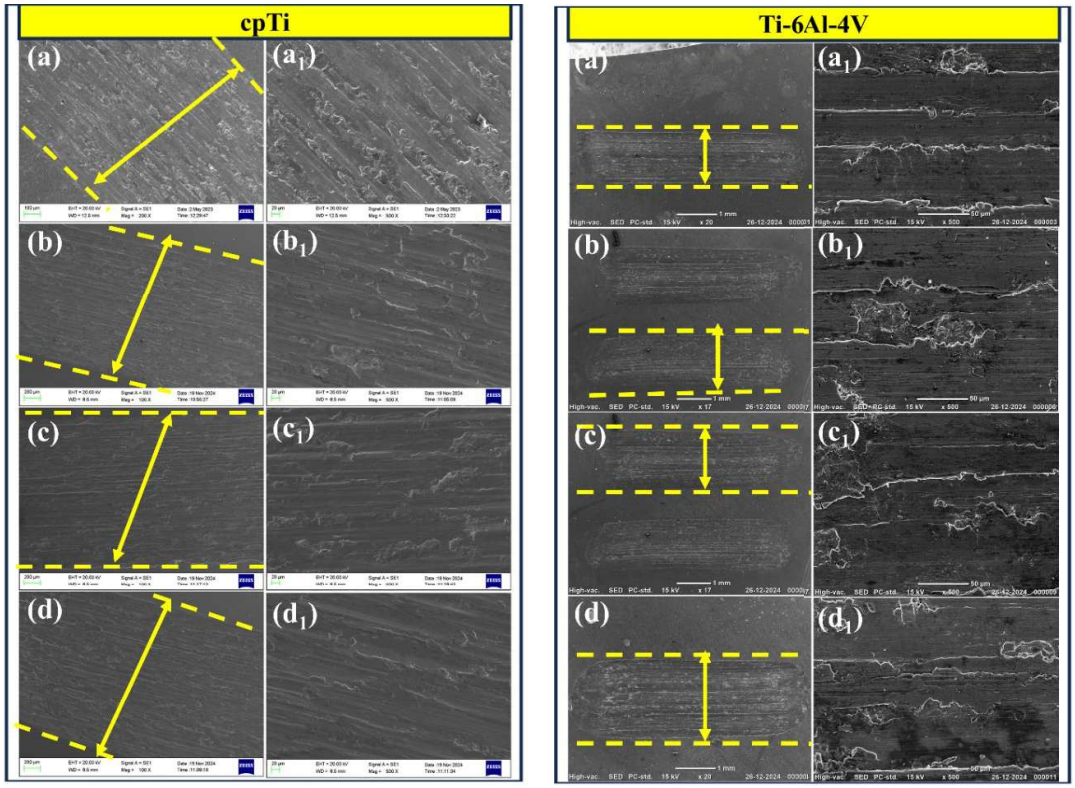

Fig. 5.31: SEM images of worn surfaces of cpTi and Ti-6Al-4V at (a)10 N, (b) 20 N, (c) 30 N, and (d) 40 N, with corresponding (a_1, b_1, c_1, d_1) at higher magnification

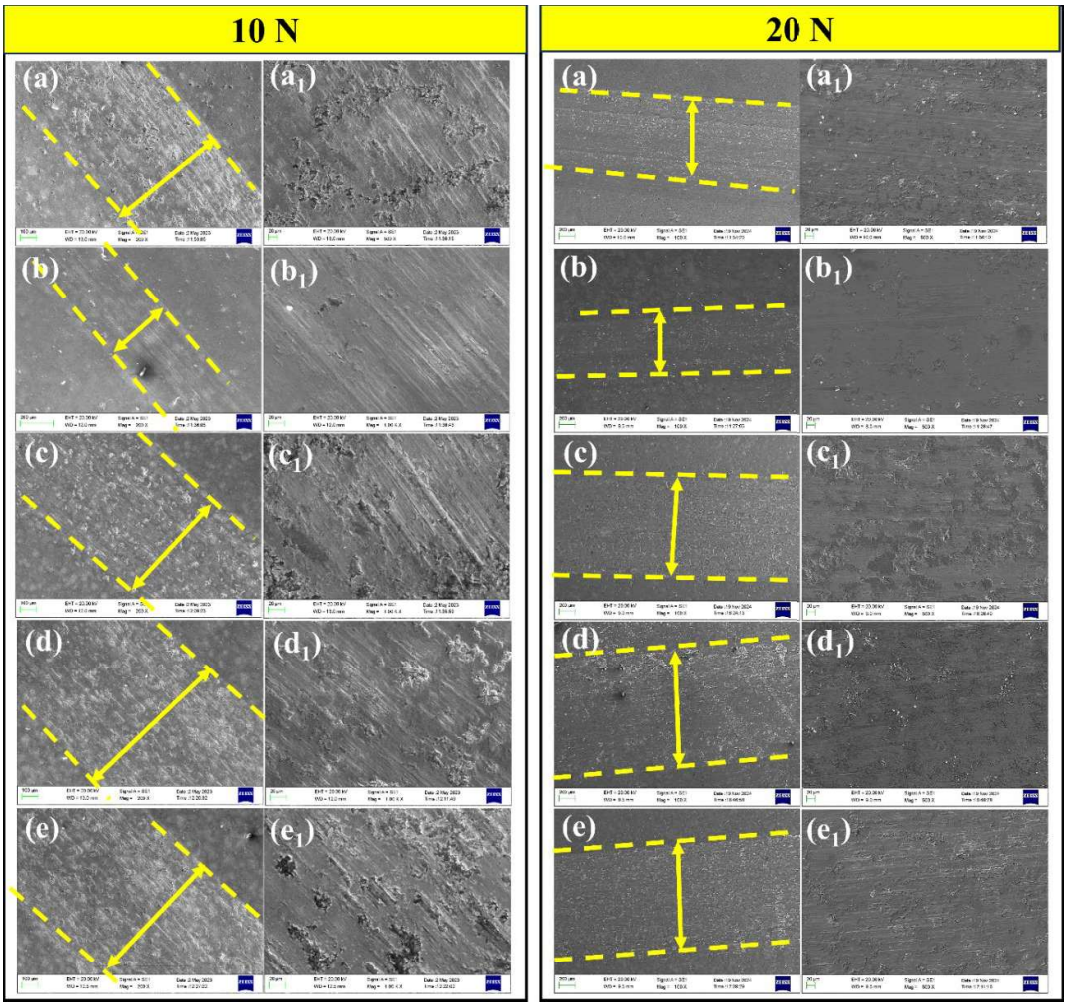

Fig. 5.32: SEM images of worn surfaces of Ti-xNb alloys at 10 and 20 N

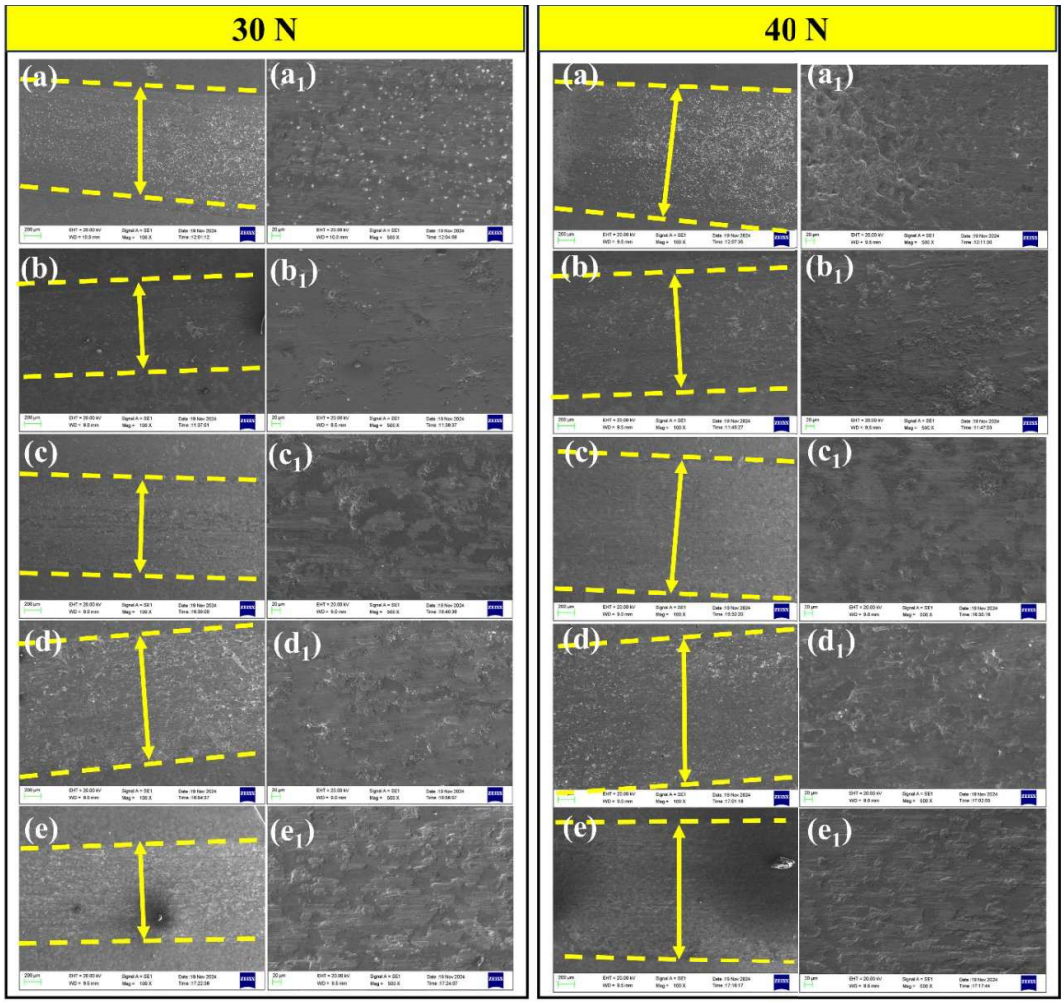

Fig. 5.33: SEM images of worn surfaces of Ti-xNb alloys at 30 and 40 N

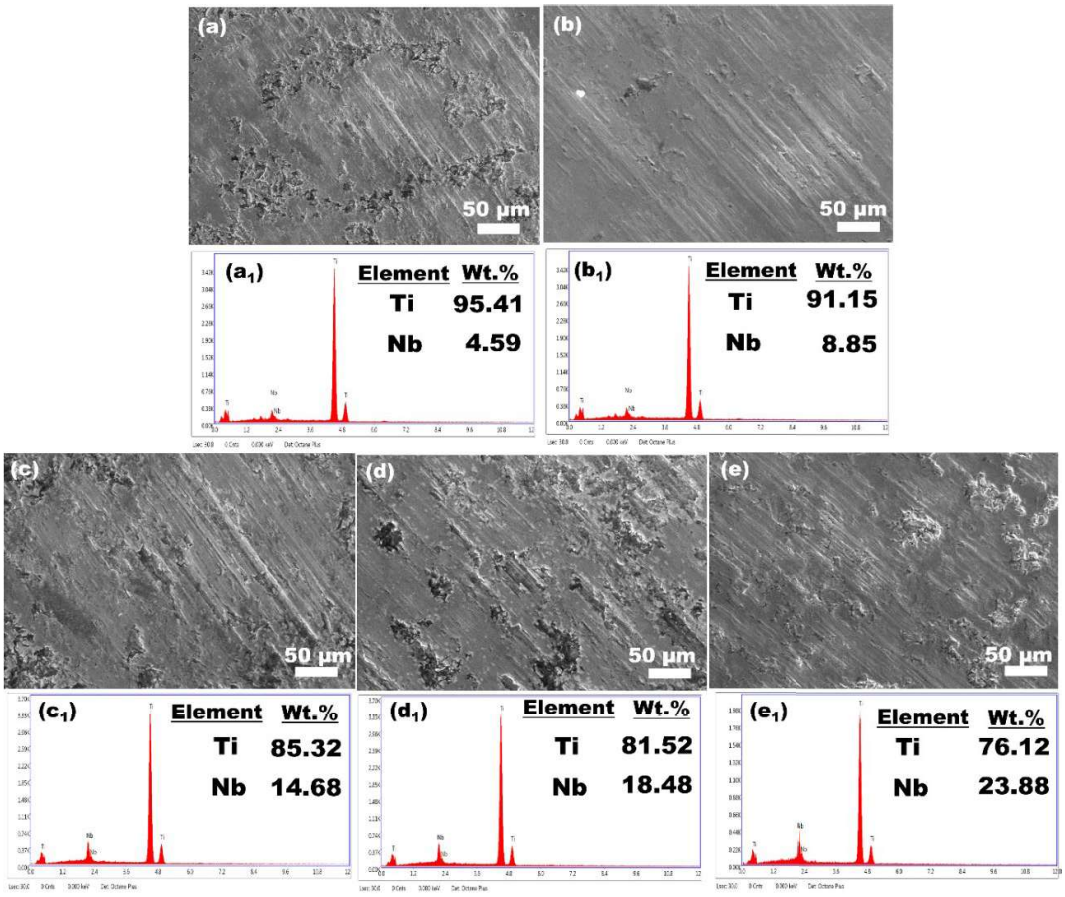

Fig. 5.34: EDS spectra of worn surfaces of Ti-xNb alloys at 10 N

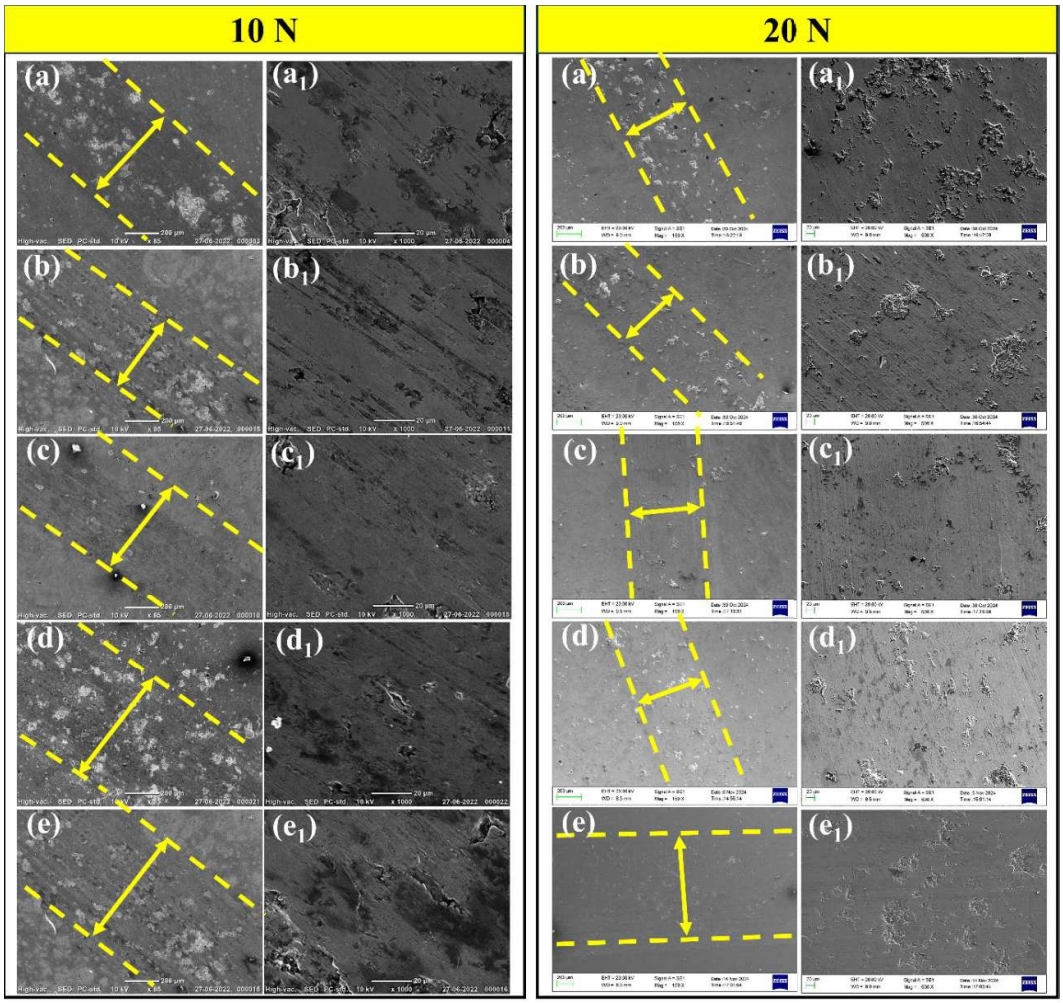

Fig. 5.35: SEM images of worn surfaces of Ti-xZr alloys at 10 and 20 N

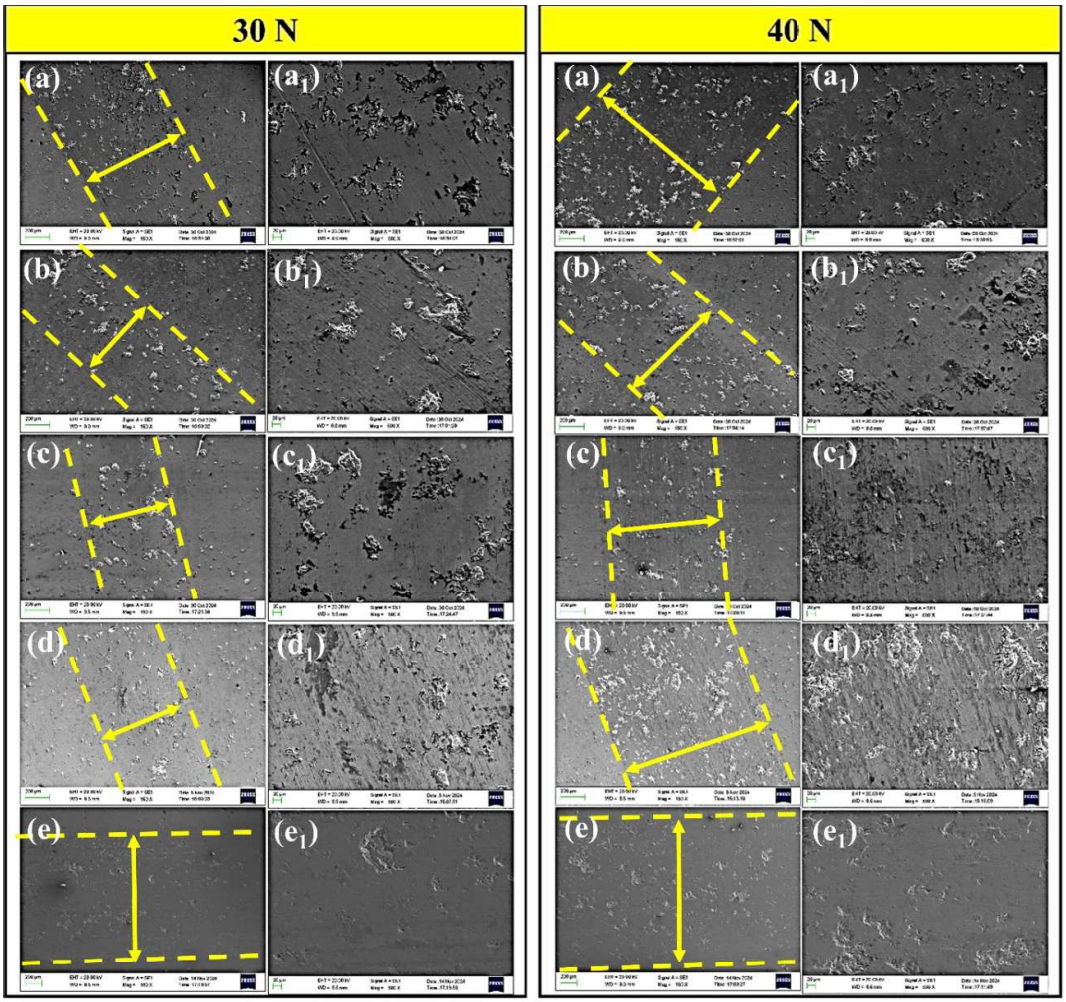

Fig. 5.36: SEM images of worn surfaces of Ti-xZr alloys at 30 and 40 N

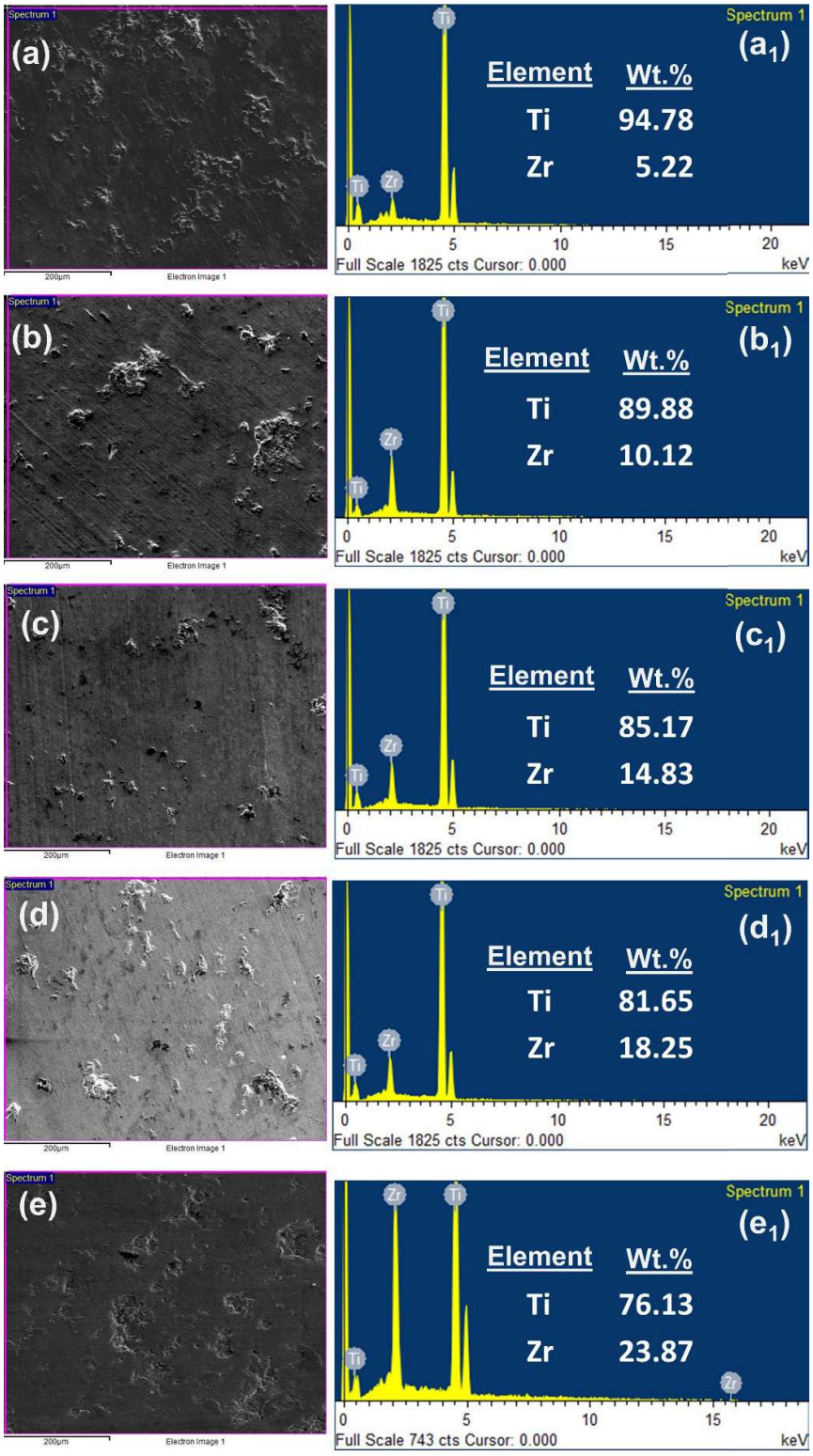

Fig. 5.37: EDS spectra of worn surfaces of Ti-xZr alloys at 10 N

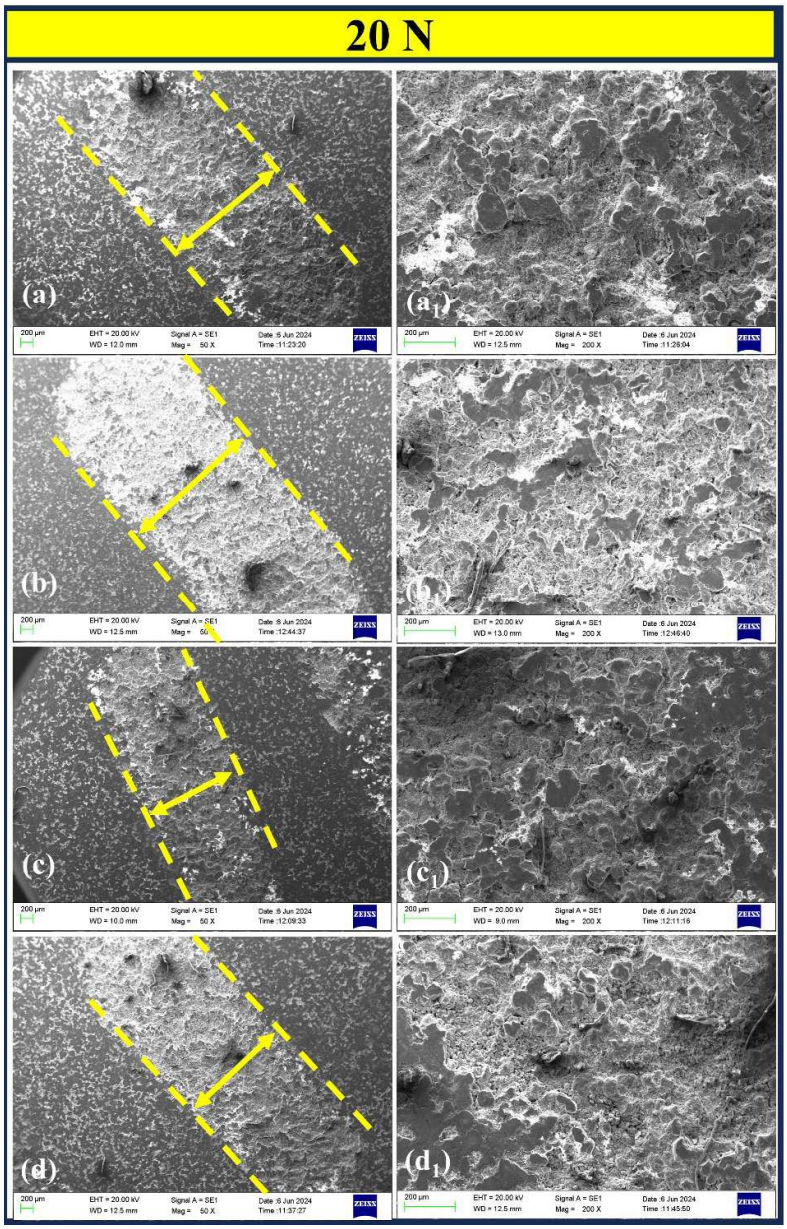

Fig. 5.38: SEM images of worn surfaces of Ti-10Zr-xNb alloys at 20 N

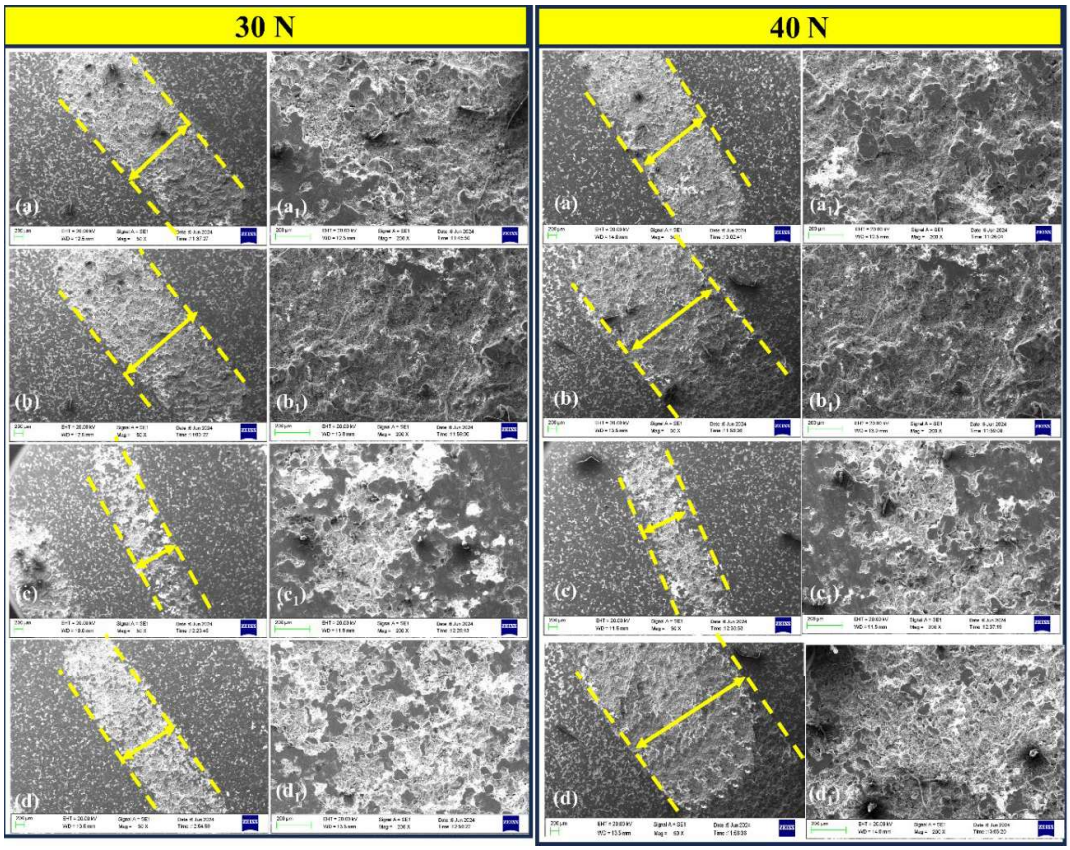

Fig. 5.39: SEM images of worn surfaces of Ti-10Zr-xNb alloys at 30 and 40 N

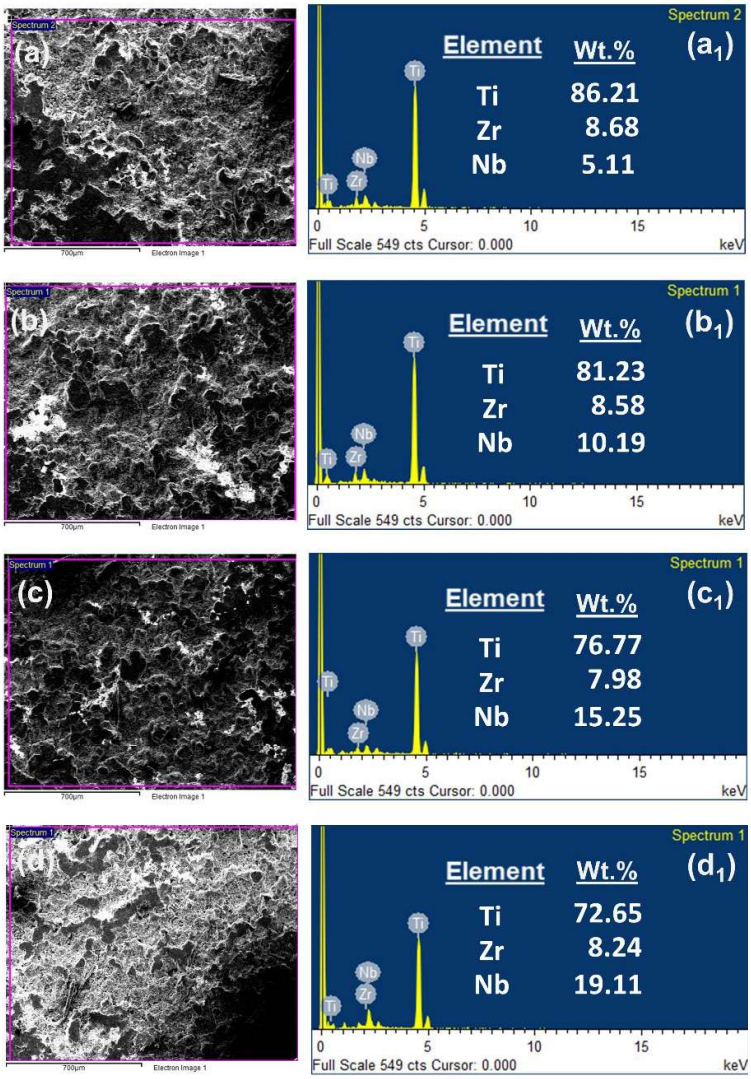

Fig. 5.40: EDS spectra of worn surfaces of Ti-10Zr-xNb alloys at 20 N

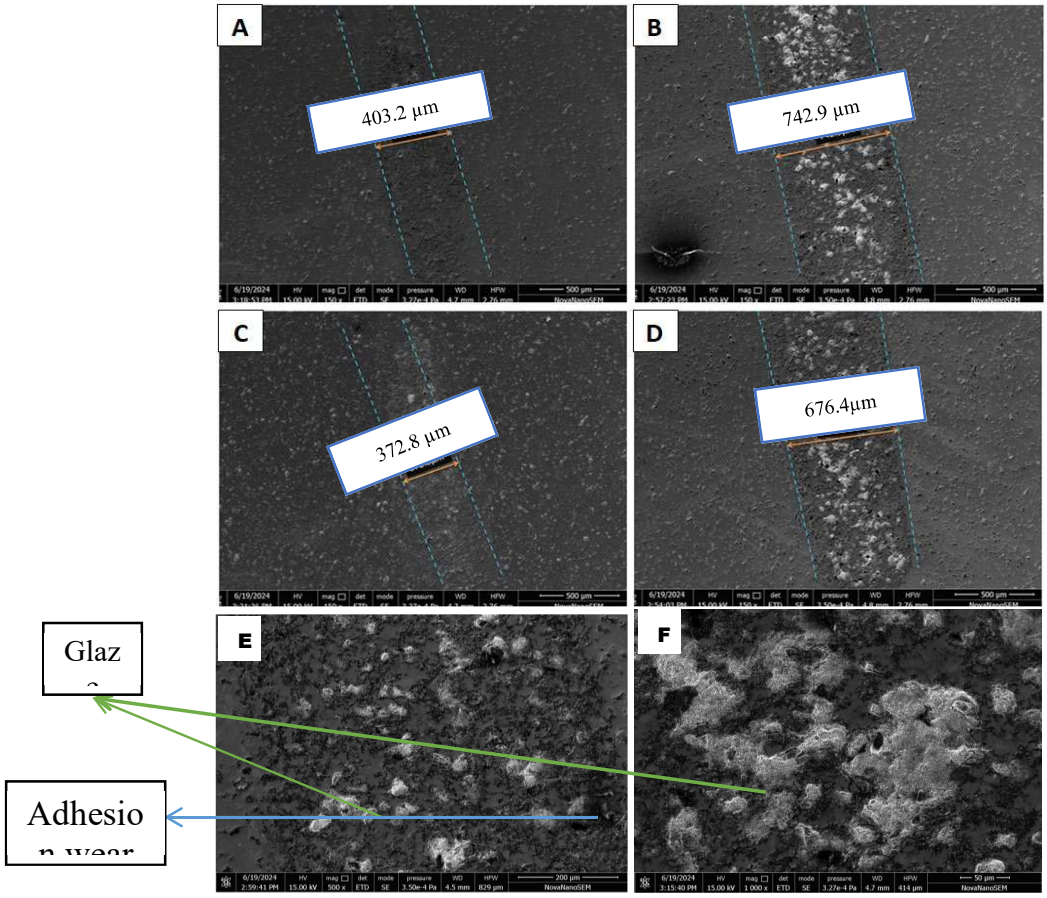

Fig. 5.41: SEM micrograph after wear of A) $TiNb_{1.5}Mo_{1.1}Zr_{1.15}Cu_{0.25}$ at 20N 150x, B) $TiNb_{1.5}Mo_{1.1}Zr_{1.15}Cu_{0.25}$ at 30N 150x, C) $TiNbZr_{0.8}Mo_{0.92}Sn_{0.28}$ at 20N 150x, D) $TiNbZr_{0.8}Mo_{0.92}Sn_{0.28}$ at 30N 150x, E) $TiNb_{1.5}Mo_{1.1}Zr_{1.15}Cu_{0.25}$ at 1000x, F) $TiNbZr_{0.8}Mo_{0.92}Sn_{0.28}$ at 1000x

5.3 Summary of the chapter

This chapter comprehensively examined the corrosion resistance, wear performance, and tribological response of commercially pure titanium (cpTi), Ti-6Al-4V, binary Ti-based alloys (Ti-Nb and Ti-Zr), ternary Ti-10Zr-xNb alloys, and high entropy alloys (HEAs) under SBF conditions, aiming to evaluate their suitability for biomedical implant applications.

In terms of corrosion performance, cpTi exhibited excellent resistance with a corrosion rate (CR) of 0.0063 mm/year. Among the binary Ti-Nb alloys, Ti-5Nb showed a comparable CR of 0.0075 mm/year, while increasing Nb content led to a progressive rise in corrosion rates, reaching a maximum of 0.082 mm/year for Ti-20Nb. Ti-Zr alloys significantly outperformed both cpTi and Ti-Nb systems, with Ti-20Zr recording the lowest corrosion rate of 0.00129 mm/year, indicating enhanced passivation characteristics of Zr. Conversely, ternary Ti-10Zr-xNb alloys showed inferior corrosion resistance, with Ti-10Zr-5Nb and Ti-10Zr-20Nb displaying CR values of 0.207 mm/year and 1.093 mm/year, respectively, attributed to destabilized passive films due to excessive β-phase content. The HEA-Cu alloy demonstrated moderate corrosion behavior with a corrosion current density of 5.281 $\mu A/cm^2$. Overall, passive film formation dominated the corrosion mechanism across all compositions.

Regarding wear performance, cpTi exhibited moderate resistance with wear volumes of 0.103 mm^3 at 10 N and 0.606 mm^3 at 40 N. Ti-6Al-4V showed comparable behavior, with wear volumes of 0.152 mm^3 at 10 N and 0.541 mm^3 at 40 N. Binary Ti-Nb alloys, particularly Ti-10Nb, showed enhanced wear resistance with values of 0.038 mm^3 at 10 N and 0.204 mm^3 at 40 N, supported by microstructural strengthening and balanced α+β phase content. The Ti-Zr series demonstrated superior performance, with Ti-15Zr showing the lowest wear volume of 0.0044 mm^3 at 10 N and 0.0435 mm^3 at 40 N due

to structural homogeneity and refined microstructure. Among ternary alloys, Ti-10Zr-15Nb exhibited the best wear behavior, recording 0.04 mm^3 at 20 N and 0.15 mm^3 at 40 N, while wear resistance deteriorated at higher Nb content. High-entropy alloys outperformed all other systems, with HEA-Sn and HEA-Cu showing minimal wear volumes. HEA-Sn recorded the lowest values of 0.004 mm^3 at 20 N and 0.0276 mm^3 at 30 N, followed closely by HEA-Cu at 0.0061 mm^3 and 0.036 mm^3, respectively, highlighting their excellent resistance due to multiphase structures and solid solution strengthening.

In conclusion, Ti-20Zr from the binary alloys demonstrated the best corrosion resistance, while Ti-15Zr excelled in wear performance. Among the ternary systems, Ti-10Zr-15Nb offered a good balance of corrosion and wear properties. Overall, the high entropy alloy HEA-Sn emerged as the most promising candidate for biomedical implant applications, exhibiting both outstanding corrosion resistance and superior tribological properties under physiological loading conditions.